Journal of Materials Chemistry A

ROYAL SOCIETY OF CHEMISTRY

REVIEW

View Article Online
View Journal | View Issue

Cite this: J. Mater. Chem. A, 2024, 12, 4421

Dimensional diversity (0D, 1D, 2D, and 3D) in perovskite solar cells: exploring the potential of mixed-dimensional integrations

Xin Li,†[ab] Sikandar Aftab,†*[c] Sajjad Hussain,[d] Fahmid Kabir,[e] A. M. A. Henaish,[fg] Abdullah G. Al-Sehemi,[hi] Mohan Reddy Pallavolu*[j] and Ganesh Koyyada*[jk]

Perovskite solar cells (PSCs) are promising photovoltaic (PV) technologies due to their high-power conversion efficiency (PCE) and low fabrication cost. This review article delves into the changing PSC landscape by analyzing the various dimensional diversity, which includes zero-dimensional (0D), one-dimensional (1D), two-dimensional (2D), and three-dimensional (3D) structures, and exploring the potential of mixed-dimensional integrations to improve the stability and performance of these promising PV devices. To fine-tune the properties of perovskite materials, researchers have used cutting-edge methods like passivation strategies, interface engineering, and exact crystal growth control. As a result, significant improvements in open-circuit voltage (V_{OC}), long-term stability, and PCE have been made. This thorough review also discusses the complex trade-offs involved in each dimensional integration, offering important insights into the complex interplay between material properties, device architecture, and fabrication techniques. Dimensional diversity in PSCs ultimately represents a dynamic path toward advancing the state-of-the-art in PV technology, providing invaluable direction to scientists and engineers attempting to realize the full potential of these next-generation solar cells. In conclusion, this review article offers a thorough analysis of the developments, difficulties, and potential of perovskite-based solar cells. It contributes to the knowledge and development of high-efficiency PSCs that hold great promise in the race for better photovoltaic performance by looking at printing techniques, stability issues, applications, and the special properties of perovskite materials.

Received 12th November 2023
Accepted 2nd January 2024

DOI: 10.1039/d3ta06953b

rsc.li/materials-a

1. Introduction

Recently, perovskite solar cells (PSCs) have received interest because of their potential to revolutionize the photovoltaic (PV) industry.[1–17] The power conversion efficiencies (PCEs) of PSCs have been demonstrated to be impressive, exceeding 25% under lab conditions.[18,19] This efficiency level is on par with commonly used traditional silicon-based solar cells.[20] The high efficiency of PSCs holds excellent promise for better-utilizing sunlight to generate electricity.[20] PSCs can be produced at a low cost and on a large scale using spin coating and inkjet printing.[21–24] They might be less expensive. Compared to traditional silicon solar cells, which require energy- and high-temperature manufacturing procedures,[25] the lower manufacturing costs of PSCs might lead to more affordable solar energy systems.[25–28] Perovskite materials are incredibly adaptable for solar cell applications due to their exceptional optical and electronic characteristics.[29–36] There have been significant improvements in perovskite materials' stability, scalability, and durability. With continued research and development, PSC's long-term stability and performance are anticipated to advance, bringing them closer to commercial viability.[37–40] They can be modified to absorb different sunlight wavelengths, including visible and infrared light.[41–43] PSCs can be transformed into flexible, lightweight components, opening up new applications for wearable electronics, building materials, and portable electronics.[44] PSCs have come a long way since they were first discovered in the field

[a]State Key Laboratory of Pulsed Power Laser Technology, National University of Defense Technology, Hefei 230037, Anhui, China
[b]Anhui Laboratory of Advanced Laser Technology, Hefei 230037, Anhui, China
[c]Department of Intelligent Mechatronics Engineering, Sejong University, Seoul 05006, South Korea. E-mail: aftab@sejong.ac.kr
[d]Department of Nanotechnology and Advanced Materials Engineering, Sejong University, Seoul, South Korea
[e]School of Engineering Science, Simon Fraser University, Burnaby, British Columbia V5A 1S6, Canada
[f]Physics Department, Faculty of Sciences, Tanta University, Tanta 31527, Egypt
[g]NANOTECH Center, Ural Federal University, Ekaterinburg 620002, Russia
[h]Research Center for Advanced Materials Science (RCAMS), King Khalid University, Abha 61413, Saudi Arabia
[i]Department of Chemistry, College of Science, King Khalid University, Abha 61413, Saudi Arabia
[j]School of Chemical Engineering, Yeungnam University, Gyeongsan 38541, Republic of Korea. E-mail: pmreddy@yu.ac.kr
[k]Department of Chemistry, Koneru Lakshmaiah Education Foundation, Vaddeswaram, Guntur, Andhra Pradesh 522302, India. E-mail: ganeshkoyyada@gmail.com
† These authors contributed equally.

in 2009.[13,45–51] PSCs can relatively quickly achieve energy payback times or the period it takes a solar panel to produce the same amount of energy used in its production.[26] Due to their high efficiency and low production energy needs, PSCs may have a shorter energy payback period than other solar cell technologies, increasing their environmental sustainability.[26,52–55] PSCs are very promising, but challenges remain to be solved like scabble synthesis of other materials with greater output,[56–59] particularly regarding long-term stability, scalability, and commercialization.

So far, several studies have been carried out, each of which has concentrated on a different facet of zero-dimensional point-spread functions (0D PSCs). In order to improve PV performance, Zhu *et al.*[60] first investigated the significance of precise phase control in all-inorganic $CsPbBr_3$ PSCs, highlighting the negative impact of 0D Cs_4PbBr_6 phases and proposing a straightforward multi-step solution-processable spin-coating method. Next, Huisman *et al.*[61] explored the transformation of 0D mixed-halide hybrid organic-inorganic $MA_4PbX_6 \cdot 2H_2O$ into 3D perovskite phases through thermal annealing, demonstrating the potential for versatile phase transitions. Achieving high stability and performance with Au contacts, McDonald *et al.*[62] presented low-hysteresis 0D organic-inorganic hybrid solar cells based on methylammonium iodo bismuthate $(CH_3NH_3)_3(Bi_2I_9)$ (MABI). Senol *et al.*[63] investigated lead-free 0D methylammonium iodo bismuthate $(CH_3NH_3)_3Bi_2I_9$ perovskite films and discussed difficulties with photoluminescence and interface energetics. Finally, Liu *et al.*[64] presented a method for improving the efficiency and flexibility of 3D $CsPbI_{3-x}Br_x$ solar cells by improving their mechanical durability. These investigations advance knowledge of various dimensional diversity of perovskite materials and their effect on the advance of perovskite solar cell technology.

Recent developments in creating high-performance PSCs have concentrated on managing perovskite crystallization and nanostructures. The problem of surface imperfections in perovskite materials still needs to be solved. One method involves adding chemical additives like 4-chlorobenzamidine hydrochloride (CBAH) to 3D perovskite layers to form 1D perovskite nanostructures on their surface.[65] As a result, the device performs better, with a notable rise in PCE from 18.53% to 20.60%. CBAH treatment improves PSC's long-term stability under light, temperature, and moisture conditions. Another method uses 1D perovskite nanowires (1D-PNWs), which are more stable and have better PCE than conventional 3D perovskite PSCs because they are created by adding urotropin (UTP) to the perovskite precursor solution.[66] Adding 1D lead iodide wires to hybrid perovskite structures shows promising PCE values and long-term stability. These innovations can potentially advance low-dimensional perovskites in optoelectronic devices significantly, address important stability issues, and hasten the adoption of PSC technology. Additionally, using one-dimensional, vertically oriented TiO_2 nano-forests as the photoanode in PSCs has produced promising results, with improved device performance and stability that put them on par with conventional PSCs.[67] These innovations brighten the future of PSCs and their incorporation into renewable energy solutions.

Researchers are actively working on the stability and efficiency of two-dimensional (2D) and quasi-2D perovskite solar cells. Quasi-2D perovskite-based PSCs have been able to achieve PCEs of over 22% after post-treatment with amphoteric imidazolium iodide (ImI), with ImI concentration optimization enhancing voltage and the fill factor while lowering hysteresis.[68] The stability of devices undergoing ImI treatment has also significantly increased under ambient conditions. Adding NH_4SCN and vertically oriented 2D perovskite films has improved stability and efficiency, advancing commercialization.[69] The introduction of formamidinium cations has improved light absorption in 2D Ruddlesden-Popper perovskites, and compositional engineering has addressed ambient instability in formamidinium perovskite films.[70,71] Additionally, techniques like interface engineering and trap deactivation reagents have shown promise in enhancing stability. These initiatives are geared toward closing the performance gap with 3D perovskite counterparts and improving the viability of PSCs for real-world PV applications.

Perovskite films with varying dimensions are distinguished using a variety of techniques. Techniques such as X-ray diffraction (XRD) for crystal structure analysis and electron microscopy for surface morphology assessment are used for thin-film PSCs, indicating flexibility and cost-effective fabrication. Because of their greater absorption capacity, thick-film perovskite cells are usually characterized by UV-Vis spectroscopy and other spectroscopic methods. Scanning probe microscopy is one way to address problems with uniform deposition. The precise characterization of nanoscale structures in nanostructured perovskite cells, which include elements like nanowires, is made possible by techniques like transmission electron microscopy (TEM). Spectroscopic and imaging techniques are used to analyze tandem perovskite cells, which are made up of multiple materials, in order to evaluate material compatibility and integration. To summarize, a range of analytical techniques, such as XRD, electron microscopy, UV-Vis spectroscopy, and TEM, are essential for recognizing and describing perovskite films with varying dimensions, offering valuable information about their optical, structural, and morphological characteristics.

Low-dimensional materials are essential for improving the stability and performance of PSCs in a range of cell configurations, such as tandem, thick-film, thin-film, and nanostructured cells. Lead halide-based compounds such as $CH_3NH_3PbI_3$ are frequently used in thin-film applications due to their advantageous optical and electronic characteristics.[72] Thick-film perovskite cells incorporate layered structures and mixed cation compositions, such as $FA_{0.83}Cs_{0.17}Pb(I_{0.6}Br_{0.4})_3$, to improve absorption and stability.[73] Utilizing materials such as SnO_2 or TiO_2 as electron transport layers for improved charge collection, nanostructured cells make use of nanowires.[74] Low-dimensional materials, such as perovskite-silicon or perovskite–perovskite combinations, are used in tandem PSCs. To achieve desired tandem structures, design strategies include optimizing the composition and morphology of the perovskite

layers, integrating buffer layers for improved charge transport, and carefully choosing material combinations.[74] This all-encompassing strategy advances the creation of stable, high-performance PSCs in a variety of ways.

There is a substantial body of literature, and we have come across a number of interesting review articles, each of which concentrated on a particular feature or characteristic of perovskite materials including 1D materials for efficient and stable PSCs,[75] solar cells with perovskite quantum dots,[5,76–79] nanocrystals in luminescent solar concentrators,[80] metal halide perovskite nano/microwires,[81] and metal halide perovskite nanorods.[82] There are still gaps in our understanding of the potential of perovskite solar cells because none of these articles provided a comprehensive analysis of the entire dimensional spectrum. This article sought to fill in these gaps by providing a comprehensive viewpoint on the possibility of integrating different dimensions within PSC technology, constituting a significant advancement in the field's exploration (Fig. 1).

2. Zero-dimensional perovskite solar cells

The PV performance of all-inorganic $CsPbBr_3$ PSCs is primarily determined by the precise phase control of Cs–Pb–Br derivatives from 3D $CsPbBr_3$ to 0D Cs_4PbBr_6. Zhu and Jingwei *et al.* discovered that the theoretically calculated Gibbs free energies (ΔG) of different phase conversion procedures reveal the optimum precursor-to-Cs–Pb–Br derivative conversion.[60] This enables a simpler multi-step solution-processable spin-coating approach (Fig. 2a) to prevent 0D Cs_4PbBr_6 phases and improve PSC solar performance due to its large exciton. This approach avoids their earlier method's direct phase change from orthorhombic to cubic $CsPbBr_3$ perovskite by eliminating recurrent annealing in each cycle.[142] Instead, annealing is only done twice during CsBr deposition. To visually illustrate how Cs_4PbBr_6 affects charge recombination, two PSCs with $CsPbBr_3$ layers were created at $n = 10$ using the conventional method (with 0D Cs_4PbBr_6) and this streamlined multi-step method (without 0D Cs_4PbBr_6) (Fig. 2b). The PCE of PSCs using 0D Cs_4PbBr_6 is significantly decreased. This shows that the Cs_4PbBr_6-free device suppresses charge recombination, supporting the process in Fig. 2c.[60] The PSC without Cs_4PbBr_6 has a longer average charge-recombination lifetime. A novel p-type 2D $ReSe_2$ nanosheet hole booster increases the all-inorganic $CsPbBr_3$ PSC without impacting perovskite film quality (Fig. 2d). Fig. 2e shows that a band at −5.15 eV effectively increases PCE by 10.67%, with an extraordinary FF of 83.06% and a V_{OC} of 1.622 V (Fig. 2f). The PV statistical data are shown in Fig. 2g. This study gives a novel approach to stable, inorganic $CsPbBr_3$ PSC platforms and a deeper understanding of Cs–Pb–Br derivative formation preferences.

Huisman and Bas AH *et al.* created 0D mixed-halide hybrid organic-inorganic $MA_4PbX_6 \cdot 2H_2O$ *via* a solvent-free mechanochemical technique ($MA = CH_3NH_3^+$; $X = Br_{1-x}I_x$ with $0 < x < 1$).[61] Through thermal annealing (dehydration) in air, this 0D phase's hydrated structure, which has characteristic near-UV absorption properties, may be reversibly transformed into the 3D $MAPbX_3$ phase (Fig. 2h). One reason for interest in these materials is the potential to convert 0D ternary lead halides into 3D perovskites for PVs and optoelectronics. The 0D to 3D transformation is visible in UV-vis absorption spectra (Fig. 2i). The powders form an apparent absorption onset at 800 nm (or 1.55 eV) as the temperature is raised to 100 °C, as predicted for $MAPbI_3$. Additionally, after a week of cooling under ambient conditions, the absorption characteristics return to those of the 0D phase as initially synthesized. It might open the door to better comprehending the ternary metal halide phase transformations, which have only been thoroughly researched for Cs-based inorganic compounds until now.

By employing MABI to produce a 0D organic-inorganic hybrid PSC with a Bi_2I_9 bioctahedron, McDonald and Calum *et al.* were able to achieve reduced hysteresis at scan rates between 150 and 1500 mV s^{-1} without modifying the interfacial layer.[83] The *J–V* characteristics of the best solar cell are displayed in Fig. 2j. Devices made with Au contacts were more efficient than those made with Ag contacts, with the highest PCE ever recorded for devices made with Au being 0.164%, as shown in Fig. 2j. Ag devices perform poorly due to Ag's quick degradation into AgI and poor work function, which reduces the hole transport layer field. The champion cell's J_{SC} was 0.694 mA cm^{-2}. Additionally, the stability of devices constructed outdoors and then kept outside and in the dark for 21 days was examined. Fig. 2k shows the long-term durability of Ag and Au metal contact for MABI devices. After 21 days, Au contact-based MABI devices showed consistent performance with minimal degradation. The slight PCE decline after three weeks may be due to device fabrication in humid open air, moisture, and spiro-MeOTAD layer breakdown. In contrast to OTPs, MABI exhibits exceptional tolerance to moisture. Ag devices had little stability,

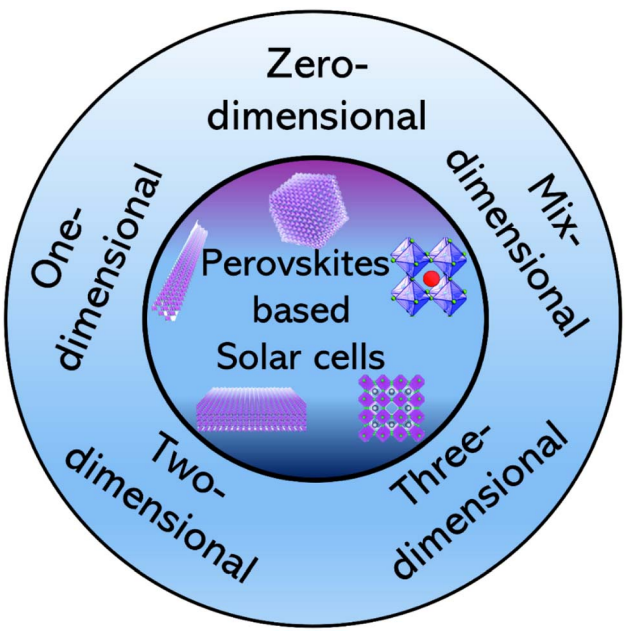

Fig. 1 Overview of our review article with dimensional diversity (0D, 1D, 2D, and 3D) in PSCs with the potential for mixed-dimensional integrations.

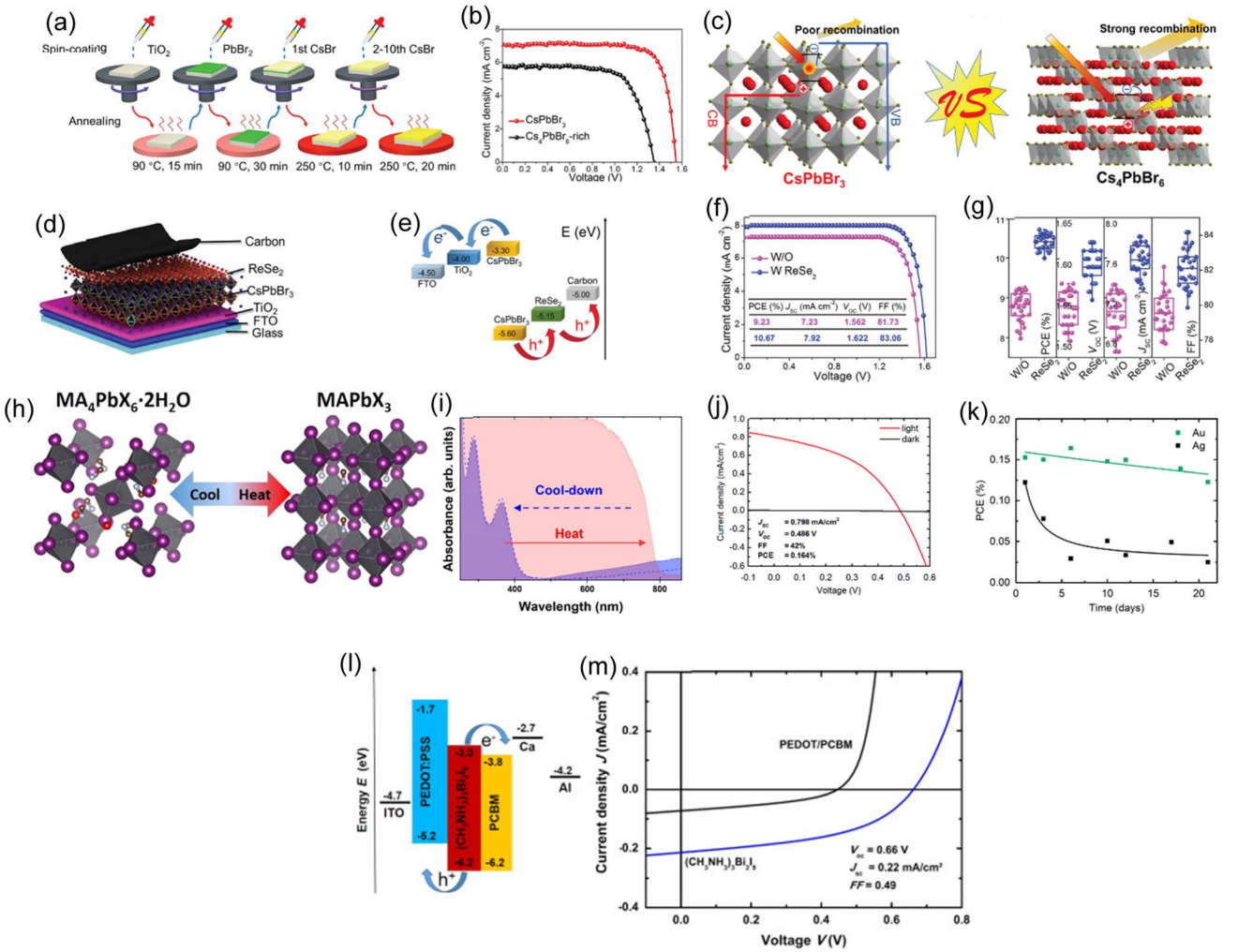

Fig. 2 (a) Schematic of the multi-step production method. (b) The J–V characteristics $CsPbBr_3$ based PSCs with and without Cs_4PbBr_6. (c) The process by which carrier recombination was induced by Cs_4PbBr_6. (d) All-inorganic $CsPbBr_3$ PSC with a $ReSe_2$-tailored structure. (e) Energy level of the all-inorganic, $ReSe_2$-tailored $CsPbBr_3$ PSC. (f) J–V curves. (g) Statistics of the PVs of different PSCs with and without $ReSe_2$. (a)–(g) Reproduced with permission.[60] Copyright 2022, Wiley. (h) In the top left corner is the crystal structure of $MA_4PbI_6{\cdot}2H_2O$, and in the top right corner is $MAPbI_3$. (i) Images illustrate the optical absorption of a pure sample of methylammonium lead iodide (blue), after thermal annealing at 100 °C (red), and after cooling to ambient temperature (blue dashes). (h) and (i) Reproduced with permission.[61] 2021, ACS. (j) J–V characteristics. (k) The stability of MABI devices with Ag and Au top contacts is plotted as a PCE with time. (j) and (k) Reproduced with permission.[83] Copyright 2017, RSC. (l) Numbers in the energy level diagram are given in relation to the vacuum. (m) J–V curves for devices with a $(CH_3NH_3)_3Bi_2I_9$ absorber (blue) and a reference cell without an absorber (black) under illumination. (l) and (m) Reproduced with permission.[63] Copyright 2016, Elsevier.

and their efficiency began to deteriorate fast after three days due to the deterioration of the Ag top contact. This study showed that MABI paired with SiNCs is a unique design that may use third-generation and carrier multiplication techniques.

0D $(CH_3NH_3)_3Bi_2I_9$ perovskite solution processed lead-free films are prepared and characterized by Senol, z, *et al.*[63] An interlayer made of a low-work function metal (calcium, 20 nm) is positioned between the PCBM and the aluminum top electrode in order to create a separation between electrons and holes in close proximity to $(CH_3NH_3)_3Bi_2I_9$. This arrangement serves to enhance the built-in voltage of the solar cell. According to the energy level diagram in Fig. 2l, the PEDOT: PSS HOMO level (at 5.2 eV) is most likely too shallow to enable effective hole absorption from the $(CH_3NH_3)_3Bi_2I_9$ absorber. Due to low interface energetics, the $(CH_3NH_3)_3Bi_2I_9$-PCBM interface may have a 0.5 eV band offset, limiting its ability to utilize the high band gap and reducing V_{OC} entirely. Additionally, the $(CH_3NH_3)_3Bi_2I_9$ perovskite absorber's relatively weak photoluminescence compared to $CH_3NH_3PbI_3$ suggests additional non-radiative recombination in the bulk of the material, which is also anticipated to result in lower V_{OC} and a poor overall PCE.[143,144] These effects can be used to explain why the Fig. 2m, $V_{OC} = 0.66$ V, is so low. The relatively low $J_{SC} = 0.22$ mA cm^{-2} shows that the exciton splitting produced by this planar device design is insufficient. This is confirmed by the high exciton binding energy (400 meV) in the 2.9 eV band gap compared to the 2.45 eV peak. The material has low PV performance, and devices have unusual PV responses that contact layers cannot explain. As shown in Fig. 2m, a device stack lacking the perovskite layer had

reduced photocurrent and V_{OC}. A more thorough investigation is required to investigate and comprehend the superior stability of 0-D perovskite.

3. One-dimensional perovskite solar cells

The creation of high-performance PSCs has undergone a radical change recently thanks to the control of perovskite crystallization and nanostructures. However, it is still unclear how to passivate perovskite surface flaws. 1D perovskites outperform bulk crystals in surface defect passivation, self-healing, and moisture stability. Wang and Jin *et al.* used CBAH as a spacer to construct orientationally crystallized nanorod-like 1D perovskite on the top surface of the 3D perovskite for surface passivation of $FAPbI_3$ perovskite.[65] Fig. 3a shows the PSC device's ITO/SnO_2/3D $FAPbI_3$-1D layer/spiro-OMeTAD/MoO_3/Ag structure. The cross-sectional SEM image in Fig. 3b shows a compact, high-quality perovskite layer. Fig. 3c shows the *J*–*V* characteristics of the best-performing PSC with and without CBAH. The control device shows 19.76% PCE, 24.662 mA cm^{-2} J_{SC}, 1.115 V V_{OC}, and 71.863% FF. After CBAH treatment, the ideal device exhibits a PCE of 21.95% with a J_{SC} of 25.000 mA cm^{-2}, a V_{OC} of 1.148 V, and an FF of 76.47%. The average PCE rises from 18.53% to 20.60% on 55 devices. PV parameter statistical distributions from the 55 devices are shown in Fig. 3d. The analysis of the unencapsulated device's long-term thermal, illumination and humidity stability with and without CBAH processing is shown in Fig. 3e. After 320 hours of illumination, the CBAH-treated PSC preserves roughly 78% of its initial PCE, much greater than the unaltered $FAPbI_3$ device (50%). The effective chemical anchoring of CBAH with PbI_2 makes perovskite layer breakdown and ion migration easier to prevent, improving device performance attenuation at 85 °C. The unencapsulated devices' moisture stability was measured under ambient conditions. After 320 hours of storage, the 1D layer exhibits significant effectiveness in thwarting moisture attacks on the perovskite device, with a 40% higher PCE than the reference device. Water-contact angle measurements show that the CBAH-containing perovskite layer's hydrophobicity improves moisture stability. Due to the 1D layer's higher hydrophobicity, the resultant perovskite showed more excellent stability under air conditions. Chemical anchoring on the perovskite surface may be a potential way to control nanostructures and orientational crystallization. This method also increases the application potential of organic halide salts.

The PSC instability issue is still an open question that prevents further commercialization of PSCs. The stability of

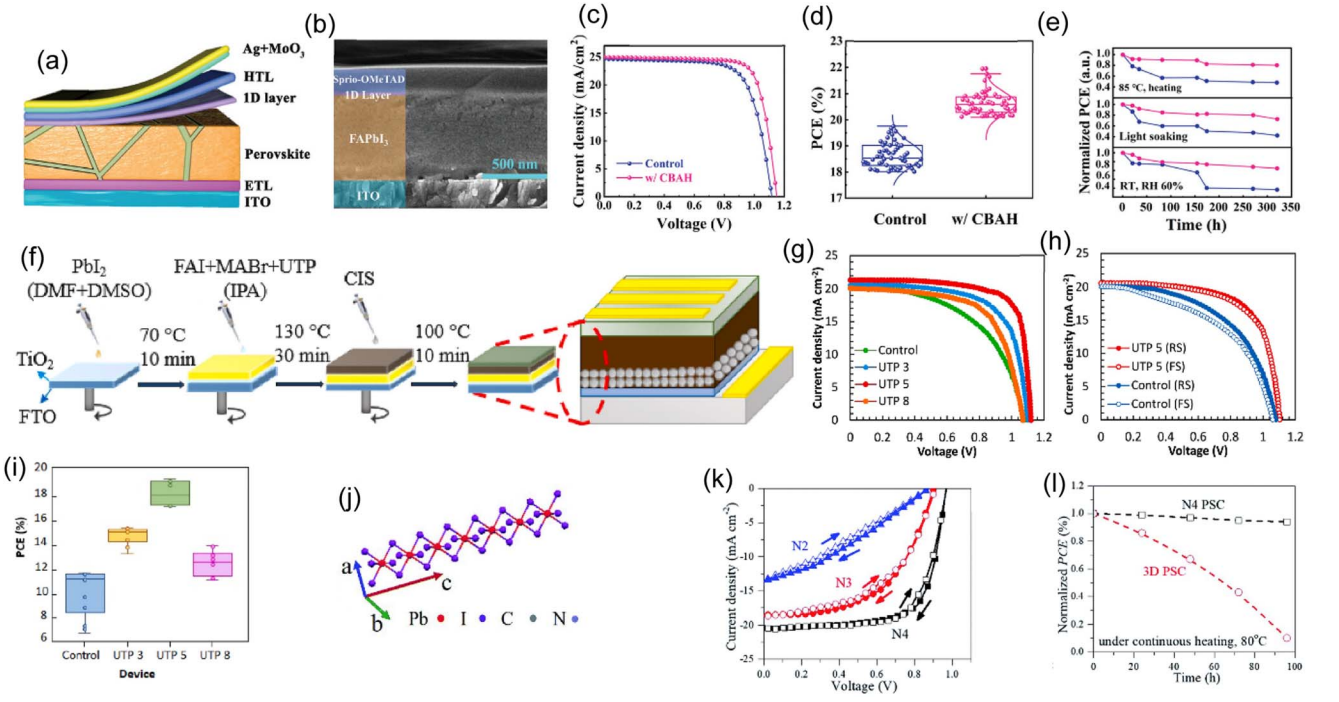

Fig. 3 (a) Schematic illustrations of the device architecture. (b) SEM cross-sectional image of the ITO/SnO_2/perovskite/spiro-OMeTAD-structured device. (c) *J*–*V* characteristics for CBAH-treated and untreated devices. (d) The statistical Voc characteristics from 55 freshly prepared devices. (e) Evolution of the PCE of CBAH-treated (red) and unencapsulated (blue) perovskite solar cells under various circumstances. (a)–(e) Reproduced with permission.[65] Copyright 2022, Wiley. (f) Schematic device architecture and two-step spin-coating process to fabricate PSCs. (g) Reverse-scanned device *J*–*V* curves. (h) *J*–*V* curves for the top-performing UTP 5 device and a control device for both the forward and reverse scans at a scan rate of 50 mV s^{-1}. (i) Devices' statistical PCE at a scan rate of 50 mV s^{-1}. (f)–(i) Reproduced with permission.[66] Copyright 2021, Elsevier. (j) An image of a single lead-iodide quantum wire. (k) Different *J*–*V* curve scan directions for N2, N3, and N4 PSCs. (l) Encapsulated N4 and 3D PSCs were heated at 80 °C and 85% RH for storage stability testing (the N4 PSC had a PCE of 13.1%). (j)–(l) Reproduced with permission.[145] Copyright 2019, RSC.

PSCs can be increased effectively by using a hybrid dimension structure created by 1D-3D. Zardari, Parisa, and Ali Rostami created self-assembled 1D-PNWs by adding UTP to the perovskite precursor in two steps to passivate grain boundaries and enhance film crystallinity.[66] GBs were passivated and self-assembled 1D-perovskite nanowires were formed in FAI and MABr organic solutions with varying UTP molar percentages. The organic solution with FAI, UTP, and MABr was spin-coated after PbI_2 was deposited on TiO_2. Fig. 3f shows device fabrication and configuration. Self-assembled 1D-PNWs passivated UTP and GB in a FTO/bl-TiO_2/mp-TiO_2/perovskite/CIS/Au PSC structure. In this investigation, control, UTP 3, UTP 5, and UTP 8 devices were produced and tested. Fig. 3g shows the reverse scan (RS) *J–V* characteristics of two-step spin-coated devices with and without UTP. Under RS measurement, the control device displays a maximum PCE of 11.47%, a V_{OC} of 1.08 V, a J_{SC} of 21.00 mA cm^{-2}, an FF of 0.63, and a Rs of 11.54 Ω cm^2. UTP improves the crystallinity, with the highest efficiency of 15.14% for UTP 3 and 19.15% for UTP 5. Fig. 3h shows the optimized and controlled PSC's *J–V* curves under various scan orientations. PCE statistics for the devices are presented in Fig. 3i. Ideal UTP 5 devices have 19.15% PCE, low hysteresis, and outstanding stability. UTP 5's PCE remained at 94.92% of its initial performance. UTP 5 had better stability than the control device due to hydrophobic alkyl groups during 1D-PNW synthesis and a moisture-resistant perovskite coating.

Ma and Chunqing *et al.* developed a low-dimensional hybrid perovskite based on 1,4-benzene diammonium lead iodide ($BDAPbI_4$).[145] A 1D lead iodide wire is formed by two lead ions six-coordinated in an octahedral geometry and linked by two surrounding ones *via* four iodine anions by the edge (Fig. 3j). This 1D lead iodide wire differs from 2D and 3D metal halide perovskite's corner-sharing PbI_6 units.[146] The PSCs have minor *J–V* hysteresis, and the N4 sample has the greatest PCE of 14.1%, followed by the N3 and N2 samples at 9.0 and 3.8%, respectively (Fig. 3k). For comparison, the 3D $MAPbI_3$ PSC is also characterized along with the stability of the encapsulated N4 PSC. After each *I–V* measurement, the devices were stored at room temperature without light (at RH = 85%). Every 100 hours, the measurements were taken again. Fig. 3l displays the normalized PCE as a function of storage time. The 3D PSC PCE drops to 70% after 1000 hours. The N4 PSC, on the other hand, still had 95% of its original PCE after 1000 hours. The development of widespread applications of 1D perovskites in optoelectronic devices will be sped up by this understanding of 1D perovskites and how it affects the performance of optoelectronic devices.

4. Two-dimensional perovskite solar cells

Quasi-2D perovskites have drawn interest because of their environmental stability compared to their 3D counterparts. Zhang, Yalan, and Nam-Gyu Park have developed a quasi-2D PSC using a multidimensional hybrid $GA(MA)_nPb_nI_{3n+1}$ ($n = 5$) alternating cation perovskite with a PCE of over 22% after post-treatment with amphoteric imidazolium iodide (ImI).[68] Fig. 4a shows the construction of planar PSCs with a FTO/c-TiO_2/perovskite/spiro-MeOTAD/Au architecture using optimized (2 mg mL^{-1} ImI treated) and unaltered films. The best device's *J–V* curves under standard conditions are shown in Fig. 4b. As the ImI concentration rises from 0 to 1, 2, 4, and 7 mg mL^{-1}, the average PCE improves. Specifically, PCEs rose from 21.36% ± 0.28% to 21.72% ± 0.29%, 20.76% ± 0.40%, and 18.19% ± 0.83%. Devices with low ImI (1 and 2 mg mL^{-1}) have improved performance due to higher V_{OC} and FF. The hysteresis index (HI) for 1 and 2 mg mL^{-1} ImI decreased from 0.033 to 0.025 and 0.015, respectively. This shows that the low-concentration-ImI treatment reduces underlying charge accumulation, which affects the HI.[147] PSC device treated with 2 mg mL^{-1} has an excellent PCE of 22.26% with a J_{SC} of 22.99 mA cm^{-2}, a V_{OC} of 1.19 V, and an FF of 0.8107. Fig. 4c illustrates the recorded stabilized power output over 325 seconds at the maximum power point (MPP). The steady-state PCE of 21.83% confirms the 2 mg mL^{-1} optimized device's efficiency. Additionally, the ideal ImI treatment improves the stability and performance of the device (Fig. 4d). For 50 days (1200 h), the 2 mg mL^{-1} treated $GA(MA)_nPb_nI_{3n+1}$ ($n = 5$) device lost less than &% of its original efficiency at RH = 25% at 25 °C. The pristine PSC device lost less than 10% of its initial efficiency under the same conditions, somewhat less than the device treated with ImI. Like expected, the 3D $MAPbI_3$-based PSC declines (18.34% of the original PCE remains after 50 days).

It is challenging to increase the PCE of 2D PSCs. The 2D perovskite film can be vertically oriented to increase the PCE. Zhang and Xinqian *et al.*[69] used a one-step spin-coating technique to create vertically oriented, highly crystalline 2D $(PEA)_2(MA)_{n-1}Pb_nI_{3n+1}$ ($n = 3, 4, 5$) films. The energy-level diagram of the planar-structured PSCs is shown in Fig. 4e. Fig. 4f displays the *J–V* curves for the PSCs with various NH_4SCN addition amounts. It is evident that NH_4SCN addition significantly improves J_{SC}, improving device performance. J_{SC} increases from 0.93 to 5.10 mA cm^{-2} when employing 1SCN (*x*SCN refers to PEAI : MAI : PbI_2 : NH_4SCN = 2 : 4 : 5 : *x*, where $x = 0, 1, 1.5, 2, 2.5, 3$)—furthermore, using 2SCN results in 15.01 mA cm^{-2}. Crystallinity improves due to perpendicular 2D perovskite layer growth on the substrate. shows PCE is a function of time at the MPP (0.86 V) and J_{SC}. A stable PCE output of 10.9% is obtained, and the J_{SC} remains stable even as the scanning duration approaches 600 s. The stability of uncapped $(PEA)_2(MA)_4Pb_5I_{16}$-based (2SCN) PSCs was evaluated at RH = 55 ± 5%. After being exposed to air for 160 hours, the device maintained 78.5% of its initial PCE, and after another 140 hours, it decreased to about 40% (Fig. 4h). The unsealed device maintained stable photovoltaic parameters for 56 days in an N_2 glove box. The outcomes offer a practical strategy for developing a highly reliable and stable PSC for potential commercialization.

Compositional engineering has solved the ambient instability and high-quality phase-pure formamidinium perovskite film fabrication problems. However, the photocurrent of the device is sacrificed due to an unfavourable increase in the bandgap. Lee Jin-Wook and colleagues developed phase-pure formamidinium-lead tri-iodide perovskite films with high optoelectronic performance and reliability.[148] The 2D hybrid perovskite formation at the 3D perovskite film's grain

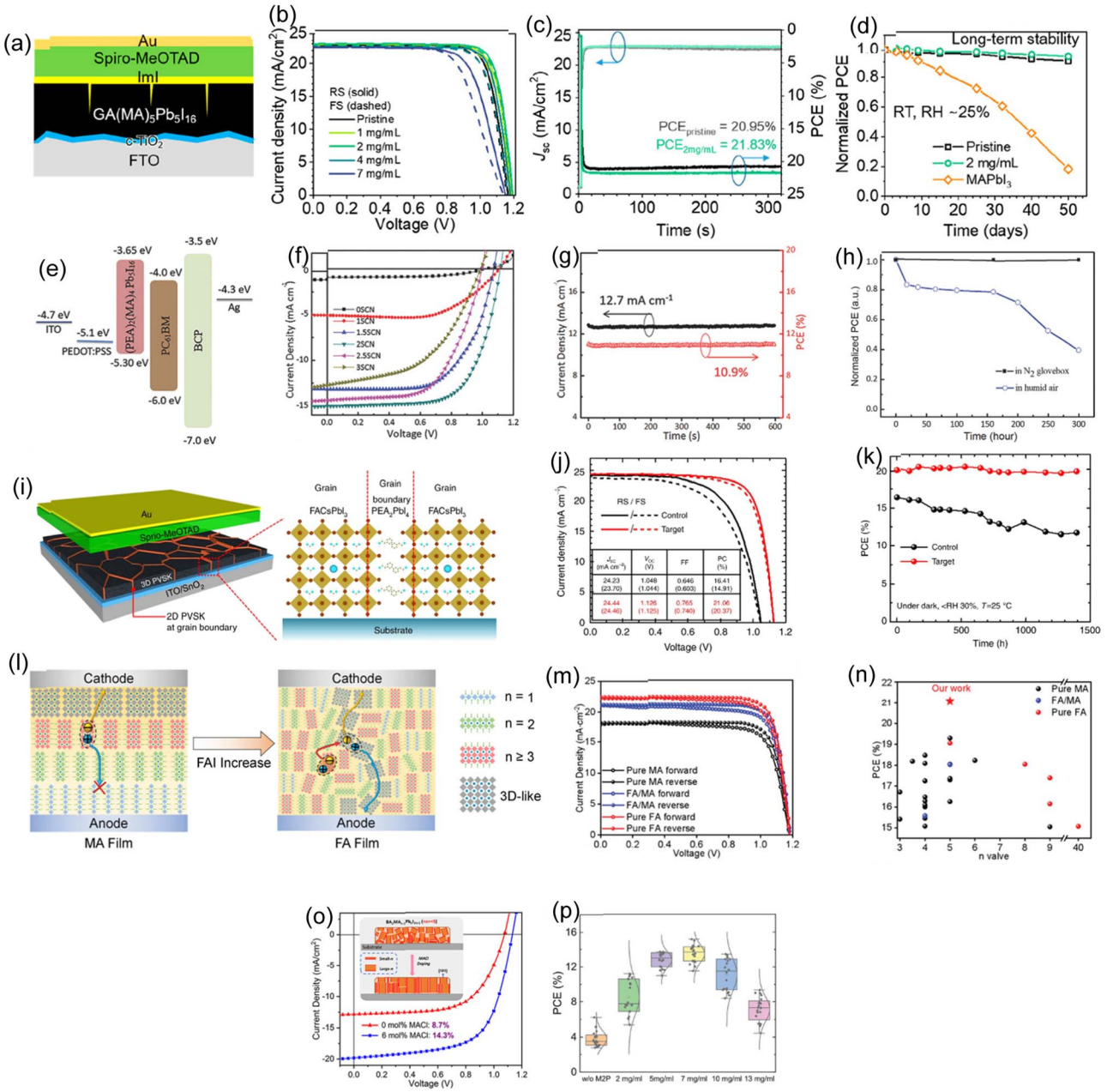

Fig. 4 (a) The quasi-2D ACI $GA(MA)_nPb_nI_{3n+1}$ ($n = 5$) based PSC device structure. (b) J–V curves of PSCs with and without (pristine) ImI treatment in both forward and reverse scans. (c) PSC's stabilized power output was measured at the MPP at a bias voltage of 0.948 V. The untreated (pristine) and treated samples contained 2 mg mL^{-1} ImI. (d) Stability of PSCs with and without (2 mg mL^{-1}) ImI treatment and PSCs based on $MAPbI_3$. (a)–(d) Reproduced with permission.[68] Copyright 2022, ACS. (e) PVSC device energy band alignment, (f) J–V curves of the devices with varying NH_4SCN concentrations, (g) PSCs' photocurrent, (h) PSC devices' stability was tested in both an N_2 glove box and an environment with a humidity of 55 5% based on the $(PEA)_2(MA)_4Pb_5I_{16}$ ($n = 5$) perovskite film. (e)–(h) Reproduced with permission.[69] Copyright 2018, Wiley. (i) Device schematics that use a polycrystalline 3D perovskite film with 2D perovskites at the grain boundaries. (j) J–V curves. (k) Evolution of the PCE of the target and control. The devices were kept in a controlled-humidity environment that was dark. (i)–(k) Reproduced with permission.[148] Copyright 2018, Nature. (l) MA and FA-based schematics of 2D perovskites' crystal orientation and phase distribution in oblique and graded vertical alignments. (m) J–V curves for the best pure MA, FA/MA, and pure FA devices while scanning forward and backward. (n) High-efficiency, low-dimensional perovskite solar cell PCE is summarised. (l)–(n) Reproduced with permission.[70] Copyright 2022, Wiley. (o) J–V curves for 0 and 6 mol% MACl PSC champion devices. The inset schematic shows how MACl doping changes stacked perovskite films. Reproduced with permission.[149] Copyright 2020, ACS. (p) PCE statistics of PSCs that did not contain spiro-OMeTAD, broken down according to the different conditions of M2P precursor solution. Reproduced with permission.[150] Copyright 2020, Wiley.

boundaries is depicted schematically in Fig. 4i. Fig. 4d shows the optimized control and target device's J–V curves. The target device's highest PCE was 21.06% (V_{OC}: 1.126 V, J_{SC}: 24.44 mA cm^{-2}, and FF: 0.765), whereas the control device's was 16.41% (V_{OC}: 1.048 V, J_{SC}: 24.23 mA cm^{-2}, and FF: 0.646). The stability of the target and control devices was contrasted. The PCE changes

of the unencapsulated devices kept in a desiccator (RH < 30%) are shown in Fig. 4k. The target device maintained 98% efficiency over 1392 hours, while the control device lost 29%. Using spontaneously produced grain boundary 2D hybrid perovskites to obtain stable and long-lasting record PCEs will assist the research community.

2D Ruddlesden-Popper perovskites are inefficient due to low light absorption and charge transfer. Shao *et al.* created 2D PSCs of formamidinium (FA), methylammonium (MA), and mixed FA/MA.[70] The absorption range increases and the light absorption is improved by adding FA cations. Fig. 4l shows 2D contour plots of rear-excited 2D perovskite's TA spectra. The *J–V* curves of pure FA, FA/MA mixed, and optimized MA-based devices are shown in Fig. 4m. The control MA-based PSC exhibits a V_{OC} of 1.18 V, J_{SC} of 18.18 mA cm^{-2}, and FF of 79.5%, resulting in a typical PCE of 17.05%, consistent with earlier results. The PCE was increased to 20.07% with a higher J_{SC} of 21.17 mA cm^{-2} after 30% MA was replaced with FA cations. Notably, the pure FA-based 2D PSCs, which displayed a high J_{SC} of 22.45 mA cm^{-2}, V_{OC} of 1.18 V, and FF of 79.5%, achieved a champion PCE of 21.07%. Fig. 4n shows the maximum PCE for low-dimensional (n < 10) PSCs with MA, FA/MA mixed, or MA cations. These findings show that efficient and reliable RP PSCs have a bright future as they move toward commercialization.

Layered 2D Ruddlesden-Popper perovskite (RPP) films are more stable than 3D ones in PSCs. 2D perovskite phase compositional inhomogeneity and non-uniform alignment reduce 2D PSC PCE. Adding methylammonium chloride (MACl) to 2D PSCs may enhance PCE and operational stability, although its effect is unknown. Zheng and Fei *et al.* have used time-space-resolved fluorescence and absorption methods to investigate the composition and charge carrier dynamics in MACl-doped $BA_2MA_4Pb_5I_{16}$ ($\langle n \rangle = 5$) layered perovskite films.[149] Fig. 4o compares champion devices with layered perovskite sheets doped with 0 and 6 mol% MACl regarding *J–V* curves. The front surface edges of small-n perovskite flakes roughened the multilayer perovskite film, resulting in a maximum efficiency (14.3%) at 6 mol% MACl doping. Kim and Hobeom *et al.* deposited benzyl ammonium iodide (BnAI) on a 3D perovskite light absorber to promote 2D self-crystallization.[150] For the optimum precursor concentration and PCE, they introduced M2P with varied precursor concentrations into PSCs without spiro-OMeTAD (FTO/compact-TiO_2/mesoporous TiO_2/SnO_2/3D perovskite/M2P/Au) (Fig. 4p). The average PCE of PSCs without M2P was 3.81% but increased to 13.50% with 7 mg mL^{-1} M2P precursor solution. However, PCE declined with increasing precursor concentration. In order to pave the way for future research in the field of PSCs, it is crucial to bring attention to utilizing 2D perovskite as an HTL.

5. Three-dimensional perovskite solar cells

At the perovskite-charge transport layer interfaces, defect-mediated carrier recombination limits the efficiency of most cutting-edge PSCs. In order to achieve cell efficiencies that are close to the theoretical limit, interfacial defects must be passivated. Mahmud and Md. Arafat *et al.*[109] showed a novel method of forming 2D layered perovskite by double-sided passivating bulky organic cation-based halide compounds on the surface of 3D perovskite films. Fig. 5a shows a third n-BAI layer between PMMA:PCBM and perovskite layers enabled double-sided passivation. The distribution of PCE for the manufactured devices is shown in the statistical chart boxes in Fig. 5b. Passivated (single-sided) cells perform more photovoltaically than the control PSCs. The *J–V* characteristics of the control and double-side (DS) passivated PSCs are shown in Fig. 5c at a scan rate of 50 mV s^{-1}. The control PSC exhibits moderate hysteresis, producing a reverse (forward) *J–V* scan efficiency of 20.02% (19.65%) with V_{OC} = 1.16 V (1.15 V), J_{SC} = 23.80 mA cm^{-2} (23.79 mA cm^{-2}), and FF = 72.55% (71.87%). In contrast, the champion DS PSC has 22.77% reverse scan PCE, 22.59% forward scan PCE, J_{SC} = 23.94 mA cm^{-2}, V_{OC} = 1.20 V, and FF = 79.31% and 78.56%. Additionally, compared to the control device (19.88%, V_{MPP} = 0.957 V), the DS PSC displays a higher steady-state PCE (22.60%) at MPP voltage (V_{MPP} = 1.008 V) (Fig. 5d). To improve device performance, passivation layer coverage is increased, the 2D interlayer crystal orientation for charge collection is tuned, and the combined effects of mixed halide compounds to align energy bands and enhance chemical passivation is researched.

PSCs have transformed the production of solution-processable solar cells. This technology is less appealing because the devices contain lead, though alternative perovskite metals are being investigated as potential replacements. Ke and Weijun *et al.* developed an en-$FASnI_3$-type tin-based perovskite absorber using formamidinium.[115] Fig. 5e shows the cross-sectional SEM picture of a finished perovskite absorber solar cell with 10% en loading. Fig. 5f displays the *J–V* curves of three representative PSCs with 0, 10, and 25% en loadings. Under the reverse scan (from V_{OC} to 0 V), the neat $FASnI_3$ PSC achieved a relatively low PCE of 1.40% with a V_{OC} of 0.15 V, a J_{SC} of 23.76 mA cm^{-2}, and an FF of 38.24%. Recombination in the perovskite absorber and poor film covering may explain this low performance. However, the PSC performance is significantly enhanced when en-$FASnI_3$ is used as the absorber. When measured using a reverse voltage scan, the material with a 10% en loading had a high PCE of 6.94%, a J_{SC} of 22.29 mA cm^{-2}, a V_{OC} of 0.47 V, and an FF of 0.6641. The J_{sc} values of perovskite-based devices with and without en are comparable, while V_{OC} and FF have improved dramatically. Under the same measurement conditions, the solar cells' 25% en-loaded perovskite absorber produced a PCE of 2.34% with a J_{SC} of 7.64 mA cm^{-2}, a high V_{OC} of 0.55 V, and an FF of 0.5580%. PSCs have a greater V_{OC} as en loading increases but a lower J_{SC} because of their broader bandgap (up to 1.9 eV) and poorer carrier transport. Thus, en-$FASnI_3$ en loading significantly affects device performance. The thermal stability of the perovskite films was also examined. After annealing at 100 °C in ambient air for 40 minutes, the tidy film nearly dissolved and turned transparent. However, when exposed to the same conditions, the film containing 10% en remained black. The longevity of device performance was then examined as a function of time under standard conditions in room-temperature air (Fig. 5g). The plot demonstrates the rapid degradation of the conventional $FASnI_3$ absorber-equipped unencapsulated solar cell. After 20 minutes, the efficiency dropped from 1.28 to 0% (short circuit). However, under the same

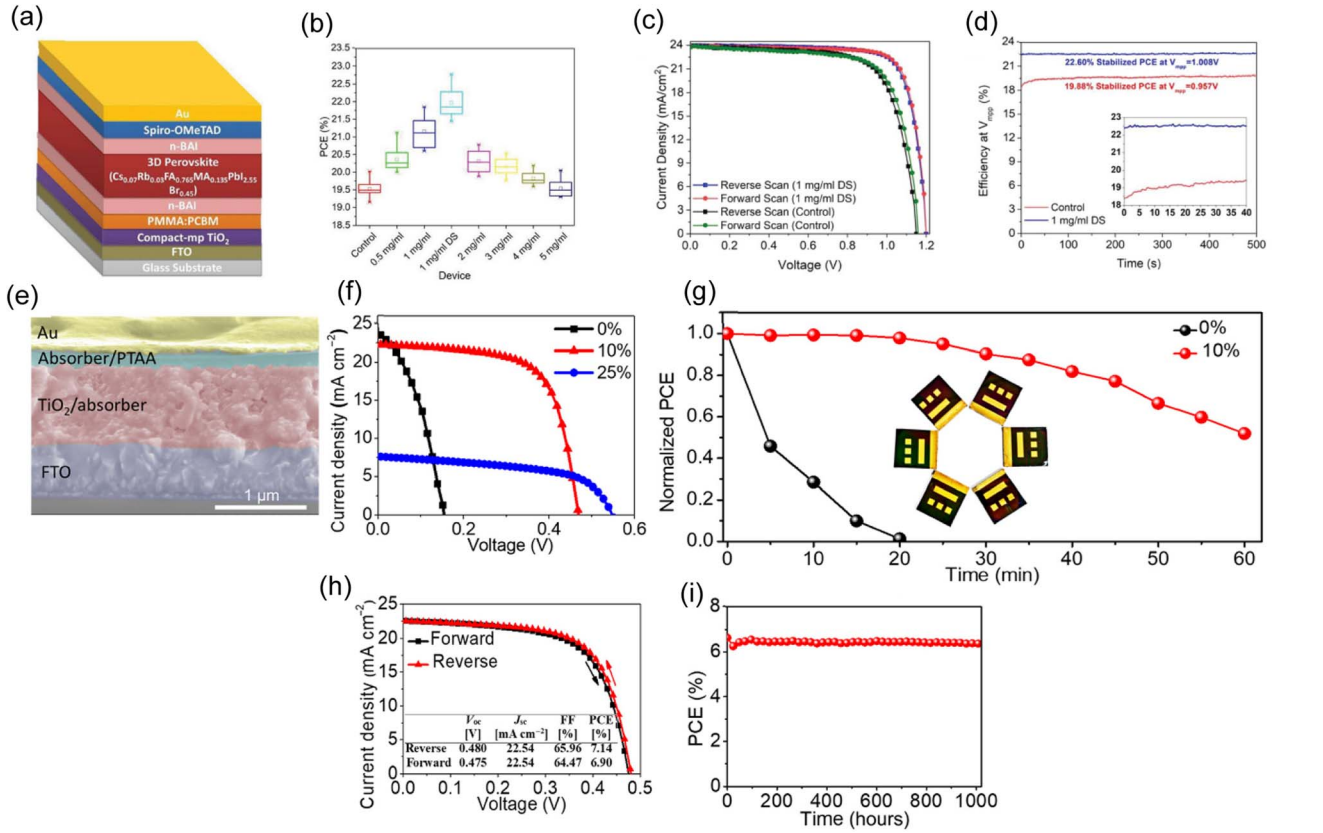

Fig. 5 (a) Diagram showing the order of the layers in a double-sided passivated PSC. (b) Plots show PCE PV parameter fluctuation for control and passivated PSCs. (c) Top-performing control and double-side passivation PSC's *J*–*V* curves. (d) Efficiency of PSCs stabilized at their MPP (the inset shows the initial 40 seconds of stabilization, showing transitory response variance between control and passivated cells). (a)–(d) Reproduced with permission.[109] Copyright 2020, ACS. (e) Cross-sectional SEM picture of the device. (f) *J*–*V* curves of perovskite absorbers added in varying amounts used in solar cells. (g) Testing the ability of solar cells to age with and without 10% loading of en-$FASnI_3$ under continuous illuminated in ambient air at AM1.5 G (air mass 1.5 global). (h) The best PSC *J*–*V* curves with 10% loading on an en-$FASnI_3$ perovskite absorber measured under forward and reverse voltage scans. (i) Efficiency of a 10% encapsulated device with storage time. (e)–(i) Reproduced with permission.[115] Copyright 2017, Science.

circumstances, the 10% en unencapsulated en-$FASnI_3$ device maintained 50% of its initial efficiency of 6.23%. Fig. 5h shows the reverse and forward voltage scan *J*–*V* curves for the best PSC with the 10% en perovskite absorber. When measured using a reverse voltage scan, this solar cell had a PCE of 7.14%, a J_{SC} of 22.54 mA cm^{-2}, a V_{OC} of 0.480 V, and an FF of 65.96%. Under the forward voltage scan, the PCE of 6.90% with a J_{SC} of 22.54 mA cm^{-2}, a V_{OC} of 0.475 V, and an FF of 64.47% shows some hysteresis. The durability of our en-$FASnI_3$ device over an extended period is tested. Fig. 5i shows that our enclosed device remains stable and efficient at 6.37% after 1000 hours. The new en-$FASnI_3$ perovskites are desirable for further enhancing the performance of lead-free devices due to their significantly increased efficiency and stability compared to neat $FASnI_3$. This method should work for lead-based PSCs and devices and Sn-based solar cells.

6. Mixed-dimensional perovskite solar cells

The exceptionally high efficiency of 3D metal-halide PSCs has been demonstrated. However, the main obstacle to industrialization is the instability of 3D perovskites. Incorporating lengthy organic cations into the crystal to end the lattice, passivate oxygen and moisture, and impede ion migration increases perovskite stability. Unfortunately, this technique frequently reduces the perovskite's ability to extract charge carriers. Due to distinct quantum confinement levels spreading bandgaps in 2D, charge-carrier localization and mobility reduction occur even in 2D-3D vertically aligned heterostructures. In order to maintain stability, a trade-off is made between PCE. When $C_6H_{18}N_2O_2PbI_4$ ($EDBEPbI_4$) microcrystals are added to the precursor solution, Li and Pengwei *et al.* found that the 3D perovskite film's grain boundaries are vertically passivated with pure 2D perovskite.[151] Fig. 6a depicts the schematic of 2D layers dotted with a 3D perovskite phase-segregated vertical heterojunction (PVHH). Fig. 6b displays the module's PV performances. Obtaining an ultra-stable, large-area, highly efficient (11.59%) PSC with the greatest documented shows excellent up-scale potential. The 2D-3D PVHH (x = 0.03) perovskite exhibited good stability in natural air ageing tests on modules (Fig. 6c). The 2D-3D PVHH perovskite module has shown greater stability with less than 10% PCE loss over 3000 h

in air. The *J–V* curve also provides excellent stability over time. The mixed 3D PSC loses over 70% PCE after 600 hours in the air, unlike the 2D-3D PVHH module. Modes underwent an accelerated aging test at RH = 65% to further test the capability. The 2D-3D-based module lost 10% of its original efficiency after 1000 h, as shown in Fig. 6d. After 600 hours, the control module lost over 90% of the original efficiency.

Gharibzadeh and Saba *et al.* produced wide-bandgap (1.72 eV) PSCs with stable PCEs up to 19.4% and an impressive 1.31 V V_{OC}.[152] Fig. 6e shows the architecture of the manufactured device on glass. The reference device (without an interlayer) displays an SPCE of 16.7% and a V_{OC} of 1.23 V under standard testing conditions for 5 minutes (see Fig. 6f and g). A layer of BABr (dissolved in isopropanol at a concentration of 2 mg

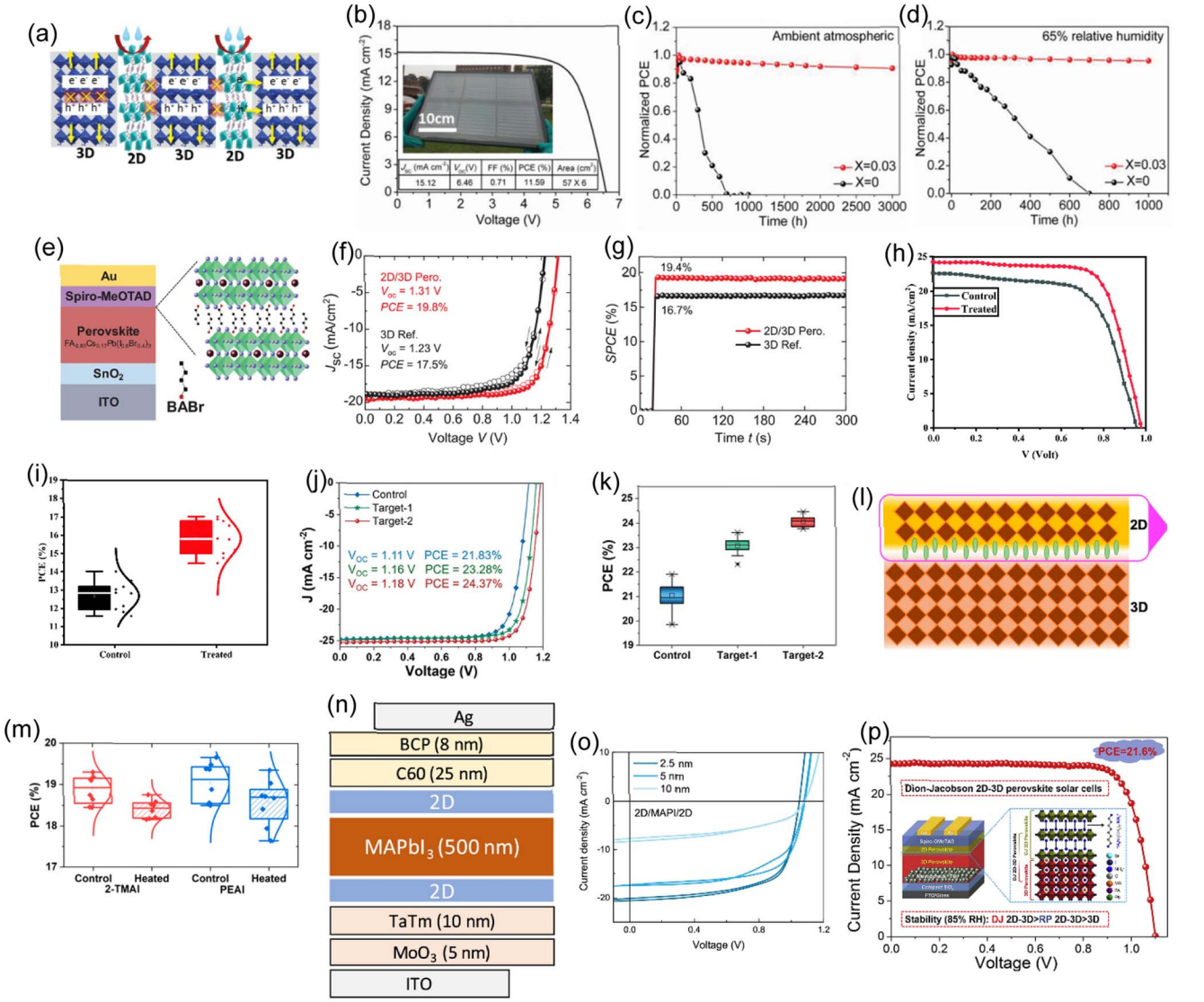

Fig. 6 (a) 2D-3D PVHH structure schematic illustration. (b) A champion module's *J–V* characteristics. An image of the module with a 342 cm^2 active area is shown in the inset. To prevent mechanical damage, the module was simply encapsulated and kept in a dark place. The stability of the module was evaluated at 65% relative (c) humidity and (d) under ambient atmospheric conditions. (a)–(d) Reproduced with permission.[151] Copyright 2018, Wiley. (e) Diagram of a solar cell made up of layers of wide-bandgap $Cs_{0.17}FA_{0.83}Pb(I_{0.6}Br_{0.4})_3$ perovskite thin-film absorbers and a 2D-RP interlayer that was made by depositing BABAr solution on top of the perovskite. (f) Reverse (open symbols) and forward (closed symbols) scans were used to determine the *J–V* characteristics of champion devices with and without a BABr (2 mg mL^{-1}) passivation layer. (g) SPCE with champion devices' continuous illumination. (e)–(g) Reproduced with permission.[152] Copyright 2019, Wiley. (h) *J–V* curves for the PSCs under the champion control and after treatment. (i) The statistical PCE distribution of every PSC under control and treatment. (h) and (i) Reproduced with permission.[153] Copyright 2021, RSC. (j) The control, target-1, and target-2 devices' *J–V* curves. (k) 50 distinct devices were used to gather statistical PCE data for the corresponding devices. (j) and (k) Reproduced with permission.[154] Copyright 2022, Wiley. (l) The left shows a 3D/2D interface graphic and a cross-sectional SEM image of the 3D/2-TMAI 2D interface. (m) Device PCE statistics comparing newly heated devices to thermally aged devices heated in accordance with the thermal cycle. (l) and (m) Reproduced with permission.[155] Copyright 2022, Wiley. (n) A perovskite heterostructure is used as the active layer in the schematics for p-i-n solar cells. (o) *J–V* curve of the 2D/MAPI/2D heterojunction solar cells for various PEA2PbI4 layer thicknesses under 100 mW cm^{-2} illumination. (n) and (o) Reproduced with permission.[156] Copyright 2019, ACS. (p) *J–V* curve. Inset shows the schematic architecture of the DJ 2D-3D perovskite. Reproduced with permission.[157] Copyright 2020, Elsevier.

mL^{-1}) was applied *via* spin-coating onto the absorber layer. This formed an interlayer between the bulk perovskite layer and the hole-transporting layer (HTL). This interlayer gives rise to a thin heterostructure comprising 2D and 3D perovskite components, predominantly the 2D-RP perovskite, which is in an intermediate phase with $n = 2$, located on the side of the perovskite solar cell responsible for hole extraction. The 2D/3D perovskite heterostructure device has a 19.8% PCE and 19.4% SPCE with minimal hysteresis during continuous one-sun irradiation (Fig. 6f and g). Dehghanipour, A. Behjat, and H. Amrollahi Bioki employed $TBABF_4$ as a passivator to improve PSC performance and stability.[153] The perovskite film's grain boundaries were passivated using $TBABF_4$ post-treatment, which reduced charge traps and engineered the perovskite/HTL interface. Fig. 6h shows *J–V* curves of treated PSCs *versus* control PSCs. Fig. 6i shows the statistical PCE distribution of every fabricated PSC. Using a two-step deposition method, Zhou and Tong *et al.* added 1-naphthalenemethylammonium iodide (NpMAI) to PbI_2 precursor solutions to control crystal formation in a 2D/3D film.[154] Fig. 6j displays the *J–V* characteristics for control, target-1, and target-2 perovskite devices using the traditional n-i-p structure, *i.e.* glass/ITO/SnO_2/perovskite/spiro-OMeTAD/MoO_3/Ag, under standard conditions. In the control device, the PCE is 21.83%, the V_{OC} is 1.11 V, the J_{SC} is 24.76 mA cm^{-2}, and the FF is 79.11%. The target-1 device's V_{OC} was significantly increased by the addition of NpMAI to the perovskite film, increasing it to 1.16 V along with a J_{SC} of 24.89 mA cm^{-2} and an FF of 80.67%, resulting in a PCE of 23.28%. The target-2 device with the $(NpMA)_2PbI_4$ perovskite layer had a V_{OC} of 1.18 V, PCE of 24.37%, J_{SC} of 25.30 mA cm^{-2} and FF of 81.36%. 2D/3D device's higher PCEs may be due to improved V_{OC}. Control devices have 70 mV lower photovoltages than target-2. Voltage may improve with better film properties and reduced non-radiative recombination loss. Under the same experimental conditions, 50 cells were independently created. The target devices 1 and 2 have improved average PCEs from the control device's 20.97% to 23.11% and 24.09%, respectively. This improvement is primarily attributable to the target device's improved average V_{OC}, which went from 1.111 V for control devices to 1.167 and 1.177 V, respectively (Fig. 6k). As shown by the target-2 device's narrower PCE distribution and higher average PCE, 2D $(NpMA)_2PbI_4$ perovskite loading in precursor solution of PbI_2 is an effective technique to make high-performance PSCs with excellent reproducibility.

A standard method for creating stable and effective perovskite solar cells is to engineer 2D/3D perovskite interfaces. 2D perovskite's main role in trap passivation has been confirmed, but its 2D/3D interface qualities under thermal stress, which commonly causes device instability, are unclear. Using *in situ* X-ray scattering, A. Sutanto *et al.* observed two typical 2D/3D interactions during a heat cycle.[155] When heated, the 2D crystalline structure dynamically evolves into a 2D/3D mixed phase, preserving the 3D bulk beneath. The sample is subjected to a thermal cycle to simulate an actual device's operational conditions, and the interface's structural evolution is tracked (Fig. 6l). Fig. 6m provides statistics on PCE. Under various treatment scenarios, the PCE of PSCs made of PEAI/3D and 2-TMAI/3D was assessed. In the control group for the PEAI/3D cells, the PCE was 19.1 ± 0.5%; after 100 minutes of heating at 50 °C, it marginally fell to 18.6 ± 0.6%. The PCE in the 2-TMAI/3D control group was 18.9 ± 0.3%, and after the same heating treatment, it slightly decreased to 18.4 ± 0.2%. The heating treatment did not significantly affect the performance of either material's solar cell because of the generally slight PCE variations within each group.

In order to improve the stability and V_{OC} of PSCs, low-dimensional (quasi-) 2D perovskites are currently the subject of extensive research. Mixing the two phases is unavoidable as only solution processing has been utilized to deposit thin 2D perovskite layers on the surface and/or grain boundaries of 3D perovskites. To examine the 3D-2D phase interaction and charge transport features of 2D perovskites in clean 2D/3D interfaces, by dual-source vacuum deposition, La-Placa and Maria-Grazia *et al.* created 2D/3D/2D perovskite heterostructures (Fig. 6n).[156] The two 2.5 nm thick 2D films had a significantly reduced FF (65.5%) despite a V_{OC} of just 6–7 meV lower than the reference (Fig. 6o). The FF fell to 49.7% as low-dimensional perovskite sheet thickness grew. Current density dropped to 8 mA cm^{-1-2} for 10 nm thick 2D sheets. The performance of different perovskite solar cell configurations was assessed using PCE, and the results reveal significant variations. Both the forward and reverse orientations of the MAPI (methylammonium lead iodide) solar cells showed respectably higher PCE values of 18.6% and 18.9%, respectively, along with respectable V_{OC} and FF. The PCE values for the 2D/MAPI/2D configuration, which ranged from 13.9% to 14.3%, were lower, indicating lower efficiency when compared to single-layer MAPI cells. Although the reverse configurations in these instances only marginally improved PCE to 18.3% and 17.7%, respectively, the 2D/MAPI and MAPI/2D configurations still showed competitive PCE values around 18.3% and 17.0% in the forward direction. These findings highlight the impact of the perovskite layer's composition and orientation on the solar cells' overall effectiveness, with MAPI exhibiting higher efficiency than the 2D/MAPI/2D configuration. Jiang and Xiaoqing *et al.* reported a more stable replacement for 3D octyldiammonium-based cations to produce a DJ 2D layer for PSCs.[157] An in situ-grown DJ 2D perovskite layer on 3D one boosts PSC stability *via* inherent stability without weak van der Waals connections and device efficiency by producing cascade HOMO levels for hole transfer and extraction. Unencapsulated DJ 2D-3D PSCs have the highest efficiency of 21.6% and great stability in 85% relative humidity, compared to RP 2D/3D and 3D (Fig. 6p). This research provides a promising method for creating stable, effective PSCs based on the DJ 2D/3D perovskite bilayer.

7. Summary and prospects

PSCs are quickly becoming recognized as highly promising PV technology due to their remarkable cost- and power-effectiveness. This thorough review article investigates the changing environment of PSCs, highlighting the significance of dimensional diversity, ranging from 0D to 3D structures, and

the potential advantages of integrating various dimensions of perovskite materials to improve stability and performance. Modern techniques have been used to meticulously optimize perovskite materials, including passivation, interface engineering, and careful control over crystal growth. This has led to appreciable improvements in long-term stability and overall efficiency. Moreover, this article provides a thorough examination of the development of high-efficiency PSCs with important ramifications for the development of PV technology in the future. Table 1 displays different PV parameters for dimensional diversity in PSCs.

Recent PSC field studies point to promising prospects and important future development directions. In order to eliminate harmful 0D Cs_4PbBr_6 phases and achieve higher PV efficiencies and long-term stability, efforts should be directed toward developing air-stable, all-inorganic $CsPbBr_3$ PSC platforms. As is shown, converting 0D mixed-halide hybrid structures into 3D perovskite phases opens up possibilities for customizing perovskite materials. Future research could focus on the mechanisms of conversion and flexible fabrication techniques. Although low-hysteresis 0D MABI-based solar cells appear promising, more device architecture and contact material optimization are required for improved efficiency and outdoor stability. Lead-free 0D methylammonium iodo bismuthate perovskite films need better interface engineering and reduced non-radiative losses for higher open-circuit voltages and efficiency. It is important to continue working on improving the mechanical durability of flexible 3D $CsPbI_{3-x}Br_x$ solar cells using 0D additives, focusing on improving additives for greater flexibility and durability, especially for wearable and portable solar applications. In order to make PSCs a workable and sustainable clean energy option, PSC research should continue to focus on stability, efficiency, scalability, toxicity, and long-term performance.

Finding a way to passivate perovskite surface flaws, addressing environmental concerns associated with lead in some perovskite materials, and finding a solution to the issue of long-term stability are some of the current challenges in the field of PSCs. Long-term stability and commercial viability continue to be major obstacles. Creating lead-free perovskite materials and enhancing scalability while maintaining high efficiency are additional ongoing difficulties. The use of 1D perovskite nanostructures and hybrid dimension structures, as well as the integration of PSCs with other PV technologies like tandem solar cells, are some future perspectives for improving PSC stability. Additionally, improvements in manufacturing processes, like using one-dimensional TiO_2 nano-forests that are vertically oriented and self-assembled NWs, show promise for enhancing performance and stability. Realizing the full potential of PSCs as a clean and effective renewable energy source requires these efforts.

PSCs are facing difficulties due to the pressing need to simultaneously improve the stability and efficiency of quasi-2D and 2D perovskite materials to compete with or outperform their 3D counterparts. The PCE displayed by 3D perovskite-based devices is still difficult for quasi-2D and 2D PSCs to achieve despite notable stability advancements. This presents a significant challenge in striking a balance between efficiency and stability. In addition to addressing the long-term stability of these advanced perovskite materials under various environmental conditions, overcoming this efficiency-stability trade-off is a challenging task. However, there is hope for the future, thanks to ongoing research into creative tactics like post-treatment techniques, compositional engineering, and trap deactivation reagents, which have significant potential to increase the stability and efficiency of quasi-2D and 2D PSCs. These initiatives promise to make these cutting-edge perovskite technologies more cost-effective than their 3D counterparts, accelerating their widespread adoption in real PV systems.

The field of 3D perovskite PSCs faces challenges related to the long-term stability and scalability of production processes and environmental sustainability by identifying substitutes for lead in perovskite compositions. Researchers are actively developing encapsulation methods to improve PSC stability over long periods. For commercial viability, developing large-scale manufacturing techniques that maintain high efficiency is essential. Research into lead-free perovskite materials and improved recycling and disposal techniques is crucial to reduce the environmental impact further. The future of perovskite solar technology is bright as it has the potential to offer a low-cost, high-efficiency renewable energy solution. However, for it to be widely used and have long-term success, these issues must be resolved.

Solar cells with 0D and 3D perovskites integrated provide a way to overcome significant field challenges. By strategically incorporating 0D perovskites, the drawbacks of 3D perovskites, such as stability issues, hysteresis, toxicity issues, and film imperfections, can be reduced. These 0D materials can stabilize, improve charge transport characteristics, and lessen toxicity and hysteresis effects. Higher efficiency, improved long-term stability, decreased environmental impact, and eventual commercialization of perovskite solar technology—which would completely alter the landscape of renewable energy—are all possible thanks to the synergy between 0D and 3D perovskites.

3D metal-halide PSCs have made impressive strides toward high efficiency, but their industrialization is hampered by a significant challenge related to the stability of 3D perovskite materials. In order to solve this problem, scientists have looked into adding long organic cations to the perovskite crystal structure. The lattice termination, moisture and oxygen passivation layer, and ion migration blockade of these organic cations all contribute to the perovskite material's increased stability. However, there is a significant flaw in this strategy. While it improves stability, it frequently comes at the expense of the perovskites' ability to extract charge carriers efficiently.

Additionally, variations in the bandgaps of the 2D perovskite layers due to quantum confinement effects in the context of 2D/3D vertically aligned heterostructures can result in charge-carrier localization and decrease carrier mobility. This trade-off between high PCE and stability preservation highlights the delicate balance scientists must strike when creating perovskite solar cells for real-world applications. It emphasizes how difficult it is to continue to improve stability and efficiency in these

Table 1 PV parameters of (0D, 1D, 2D, 3D, and 2D/3D) in PSCs

PSCs	Structure	V_{OC} (mV)	J_{SC} (mA cm^{-2})	FF (%)	η (%)	Year	Ref
0D	PEN/ITO/SnO_2/$CsPbI_3$-xBr_x/spiro-OMeTAD/Au (n-CsBr = 0 M)	0.76	11.12	52.91	4.48	2023	64
	PEN/ITO/SnO_2/$CsPbI_3$-xBr_x/spiro-OMeTAD/Au (n-CsBr = 0.3 M)	1.06	15.96	59.67	10.12	2023	64
	PEN/ITO/SnO_2/$CsPbI_3$-xBr_x/spiro-OMeTAD/Au (n-CsBr = 0.4 M)	1.01	17.82	65.77	11.93	2023	64
	PEN/ITO/SnO_2/$CsPbI_3$-xBr_x/spiro-OMeTAD/Au (n-CsBr = 0.5 M)	1.09	18.47	70.67	14.25	2023	64
	PEN/ITO/SnO_2/$CsPbI_3$-xBr_x/spiro-OMeTAD/Au (n-CsBr = 0.6 M)	1.02	17.17	64.77	11.36	2023	64
	PEN/ITO/SnO_2/$CsPbI_3$-xBr_x/spiro-OMeTAD/Au (n-CsBr = 0.7 M)	0.99	15.88	59.81	9.41	2023	64
	FTO/c-TiO_2/m-TiO_2/CsPbBr3/$ReSe_2$/carbon	1.622	7.92	83.06	10.67	2022	60
	ITO/TiO_2/$(CH_3NH_3)_3(Bi_2I_9)$/spiro-OMeTAD/Ag	0.42	0.316	32	0.042	2017	83
	ITO/TiO_2/$(CH_3NH_3)_3(Bi_2I_9)$ + SiNCs/spiro-OMeTAD/Ag	0.35	0.463	28	0.047	2017	83
	ITO/PEDOT/$(CH_3NH_3)_3Bi_2I_9$/PCBM/Ca/Al	0.66	0.22	49	0.1	2016	63
1D	FTO/c-TiO_2/m-TiO_2/$TFPbI_3$/ZrO_2/carbon	1.012	23.26	73.70	17.42	2022	84
	ITO/PTAA/$TPPbI_3$/C_{60}/BCP/Cu	1.150	24.70	81.00	22.90	2022	85
	FTO/c-TiO_2/SnO_2/EMIMPbI_3/spiro-OMeTAD/Ag	1.069	23.10	78.10	22.14	2022	86
	ITO/SnO_2/FA(CBA)PbI_4/spiro-OMeTAD/MoO_3/Ag	1.148	2500	76.47	21.95	2021	65
	ITO/SnO_2/(*m*-PBA)Pb_2I_6/spiro-OMeTAD/Au	1.155	25.32	80.88	23.84	2022	87
2D	ITO/NiOx/$FASnI_3$/PCBM/Al	0.59	14.44	69	5.94	2017	88
	ITO/PEDOT:PSS/$MASnI_3$/PCBM/LiF/Al	0.38	21.87	48.3	4.03	2019	89
	ITO/PEDOT:PSS/$FASnI_3$/C_{60}/BCP/Cu	0.45	24.87	63	7.05	2018	90
	ITO/PEDOT:PSS/$FASnI_3$/PCBM/BCP/Ag	0.54	22.64	64	7.86	2019	91
	ITO/c-TiO_2/m-TiO_2/$(BA)_2(MA)_{n-1}Sn_nI_{3n+1}$/PTAA/Au	0.229	24.1	45.7	2.53	2017	92
	ITO/PEDOT:PSS/$FASnI_3$/PCBM/BCP/Ag	0.54	20.69	69.06	7.71	2022	93
	ITO/PEDOT:PSS/perovskite/spiro-OMeTAD/Ag	0.614	20.159	68.6	8.71	2019	94
	ITO/PEDOT:PSS/$(BA_{0.5}PEA_{0.5})_2FA_3Sn_4I_{13}$/C60/LiF/Al	0.6	21.82	66.73	8.82	2019	95
	FTO/PEDOT:PSS/$FASnI_3$/C60/BCP/Ag	0.59	22.06	69	9.1	2020	96
	ITO/PEDOT/$FASnI_3$/ICBA/BCP/Ag	0.91	20.6	77.1	14.6	2021	97
	ITO/PEDOT:PSS/$(BA_{0.3}PEA_{0.7})_2FA_3Sn_4(I_{1-x}Ac_x)_{13}$/ICBA/LiF/Al	0.65	23.33	68.56	10.36	2021	98
	ITO/PEDOT:PSS/$MASnI_3$/PC61BM/BCP/Ag	0.53	19.8	65.1	6.8	2022	99
	FTO/PEDOT:PSS/$FASnI_3$/C60/BCP/Ag	0.65	22.2	71.6	10.4	2021	100
	FTO/c-TiO_2/m-TiO_2/ZrO_2/(4AMP)$FA_3Sn_4I_{13}$/C	0.64	14.9	44.3	4.22	2018	101
	FTO/Cu-NiO_x/(4AMP)$FA_3Sn_4I_{13}$/PCBM/BCP/Ag	0.69	21.15	74	10.9	2020	102
	ITO/PEDOT:PSS/(BEA)/$FA_2Sn_3I_{10}$/PCBM/Ag	0.62	18.85	56.1	6.43	2020	103
	ITO/PEDOT:PSS/$FASnI_3$/C60/BCP/Ag	0.514	21.46	68.87	7.6	2020	104
	ITO/PEDOT/(3AMP)$(MA_{0.5}FA_{0.5})_3(Pb_{0.5}Sn_{0.5})_4I_{13}$	0.88	28.63	79.74	20.09	2020	105
3D	PEN/ITO/SnO_2/perovskite/spiro-OMeTAD/Au	1.17 ± 0.02	24.05 ± 0.20	72 ± 2	20.85 ± 0.50	2022	106
	ITO/PTAA/perovskite/C_{60}/BCP/Ag	1.07	22.60	76.92	18.60	2021	107
	FTO/PEDOT:PSS/perovskite/PQDs/spiro-OMeTAD/MoO_3/Ag	1.09 ± 0.03	23.69 ± 0.59	76 ± 1	19.68 ± 0.38	2023	108
	FTO/mp-TiO_2/PMMA-PCBM/n-BAI/$Cs_{0.07}Rb_{0.03}FA_{0.765}MA_{0.135}PbI_{2.55}Br_{0.45}$/n-BAI/spiro-OMeTAD/Au	1.16	23.80	72.55	20.02	2020	109
	ITO/P3CT-K/$CH_3NH_3PbI_3$/$PC_{61}BM$/ZnO/Al	1.028	22.50	72.1	16.70	2018	110
	ITO/P3CT-K/$CH_3NH_3PbI_3$(SP-3D-COF 1)/$PC_{61}BM$/ZnO/Al	1.026	23.20	79.8	18.95	2018	110
	ITO/P3CT-K/$CH_3NH_3PbI_3$(SP-3D-COF 2)/$PC_{61}BM$/ZnO/Al	1.031	23.60	78.3	19.07	2018	110
	FTO/mp-TiO_2/$(FAPbI_3)_{0.85}(MAPbI_2Br)_{0.10}(CsPbI_3)_{0.05}$/(Me-PDA)$Pb_2I_6$/Spiro-OMeTAD/Au	1.13	24.61	79	22.0	2021	111
	PET/ITO/SnO_x/PNPs@NiOx@PAM/Spiro-OMeTAD/Au	0.98	21.80	77.56	16.57	2022	112
	PET/ITO/SnO_x/PNPs @PAM/Spiro-OMeTAD/Au	0.96	21.04	73.47	14.84	2022	112
	PET/ITO/SnO_x/PNPs@SiO_2@PAM/Spiro-OMeTAD/Au	0.97	20.67	73.12	14.06	2022	112
	FTO/TiO_2 tube/$CH_3NH_3PbI_3$/spiro-MeOTAD/Ag	0.87	11.3	63	6.2	2015	113
	FTO/TiO_2/ZnO$CH_3NH_3PbI_3$/spiro-MeOTAD/Ag	0.71	12.2	49	4.0	2015	113
	FTO/ZnO NW/$CH_3NH_3PbI_3$/spiro-MeOTAD/Ag	0.73	11.7	35	3.0	2015	113
	FTO/ALD-TiO_2 nanostructures/$CH_3NH_3PbI_{3-x}Cl_x$/P3HT/Ag (TiO_2 planar)	0.90	18.0	60.7	9.83	2016	114
	FTO/ALD-TiO_2 nanostructures/$CH_3NH_3PbI_{3-x}Cl_x$/P3HT/Ag (TiO_2 180 nm)	0.91	20.6	56.3	10.6	2016	114
	FTO/ALD-TiO_2 nanostructures/$CH_3NH_3PbI_{3-x}Cl_x$/P3HT/Ag (TiO_2 270 nm)	0.92	21.5	60.3	12.5	2016	114
	FTO/ALD-TiO_2 nanostructures/$CH_3NH_3PbI_{3-x}Cl_x$/P3HT/Ag (TiO_2 370 nm)	0.89	16.5	49.2	7.25	2016	114
	FTO/TiO_2/$FASnI_3$/PTAA/Au (7.5% en loading)	0.29	23.61	57.35	3.94	2017	115
	FTO/TiO_2/$FASnI_3$/PTAA/Au (10% en loading)	0.43	23.22	62.65	6.27	2017	115
	FTO/TiO_2/$FASnI_3$/PTAA/Au (12.5% en loading)	0.47	20.04	62.16	5.86	2017	115
	FTO/TiO_2/$FASnI_3$/PTAA/Au (15% en loading)	0.51	17.33	61.20	5.43	2017	115

Table 1 (*Contd.*)

PSCs	Structure	V_{OC} (mV)	J_{SC} (mA cm^{-2})	FF (%)	η (%)	Year	Ref
2D/3D	FTO/PEDOT:PSS/$GAMA_3Pb_3I_{10}$/PCBM/Al	0.974	9.36	79.7	7.26	2017	116
	ITO/PEDOT:PSS/$(GA)(MA)_3Pb_3I_{10}$/PCBM/Li–F/Al	1.08	20.75	74.52	16.65	2019	117
	FTO/c-TiO_2/$(GA)(MA)_3Pb_3I_{10}$/PCBM/Ag	1.15	18.8	67.8	14.7	2019	118
	FTO/c-TiO_2/$(GA)(MA)_3Pb_3I_{10}$/spiro-OMeTAD/Au	1.14	22.26	72.67	18.48	2019	119
	FTO/c-TiO_2/$(GA)(MA)_3Pb_3I_{10}$/spiro-OMeTAD/Au	1.08	22.68	78.01	19.18	2021	120
	FTO/PEDOT:PSS/$CsSnBrI_2$-PS/PCBM/BCP/Ag	0.43	17.2	68.7	5.01	2021	121
	ITO/PEDOT:PSS/$FASnI_3$/ICBA/BCP/Al	0.84	24.91	70.76	14.81	2021	122
	ITO/PEDOT:PSS/$FASnI_3$/C60/BCP/Ag	0.656	22.19	73.11	10.61	2022	123
	ITO/PEDOT:PSS/$PEA_{0.15}FA_{0.75}MA_{0.1}SnI_2Br$/PCBM/BCP/Ag	0.67	16.89	70.36	7.96	2022	124
	FTO/c-TiO_2/$(PEA)_2(MA)_2Pb_3I_{10}$/spiro-OMeTAD/Au	1.18	6.72	60	4.73	2014	125
	FTO/mp-TiO_2/$(BA)_2(MA)_2Pb_3I_{10}$/spiro-OMeTAD/Au	0.93	9.42	46	4.02	2015	126
	FTO/mp-TiO_2/$(BA)_2(MA)_3Pb_4I_{13}$/spiro-OMeTAD/Au	0.87	9.09	30	2.39	2015	126
	FTO/mp-TiO_2/$(IC_2H_4NH_3)_2(MA)_{n-1}Pb_nI_{3n+1}$/spiro-OMeTAD/Au	0.893	14.33	63	9.03	2016	127
	FTO/mp-TiO_2/mp-ZrO_2/$(AVA)_x(MA)_{1-x}PbI_3$/carbon	0.85	21.78	64	11.86	2017	128
	FTO/mp-TiO_2/$(PEA)_2(MA)_{49}Pb_{50}Br_{151}$/spiro-OMeTAD/Au	1.46	9.0	65	8.5	2017	129
	FTO/mp-TiO_2/$(PPA)_2(MA)_{49}Pb_{50}Br_{151}$/spiro-OMeTAD/Au	1.24	9.5	60	7.1	2017	130
	FTO/mp-TiO_2/$(BZA)_2(MA)_{49}Pb_{50}Br_{151}$/spiro-OMeTAD/Au	1.35	11.5	63	9.5	2017	130
	FTO/mp-TiO_2/$(EDA)(MA)_2[Pb_3I_{10}]$/spiro-OMeTAD/Au	1.24	16.57	56	11.58	2016	131
	ITO/PEDOT:PSS/$(PEI)_2(MA)_6Pb_7I_{22}$/PCBM/LiF/Ag	1.1	13.12	65	9.39	2016	132
	FTO/PEDOT:PSS/$(BA)_2(MA)_3Pb_4I_{13}$ (HC)/PCBM/Al	1.01	16.76	74	12.51	2016	133
	ITO/C_{60}/$(iso\text{-}BA)_2(MA)_3Pb_4I_{13}$ (HC)/spiro-OMeTAD/Au	1.20	16.54	53	10.63	2017	134
	FTO/m-TiO_2/$(BA)_2(MA)_3Sn_4I_{13}$/PTAA:TPFB/Au	0.23	24.1	46	2.53	2017	92
	ITO/NiO_x/$PEA_2FA_8Sn_9I_{28}$/PCBM/Al	0.59	14.44	69	5.94	2017	88
	ITO/PEDOT:PSS/$(PEA)_2(FA)_{n-1}Sn_nI_{3n+1}$/$C_{60}$/BCP/Al	0.458	22.5	58	9.0	2018	135
	ITO/PTAA/ $Cs_{0.05}FA_{0.70}MA_{0.25}PbI_3$/$C_{60}$/BCP/Cu	1.06	23.4	68.4	15.02 ± 0.78	2019	136
	ITO/PTAA/ $Cs_{0.05}FA_{0.70}MA_{0.25}PbI_3$-DAP/$C_{60}$/BCP/Cu	1.16	23.4	79.4	20.36 ± 0.46	2019	136
	ITO/PTAA/$MAPbI_3$/C_{60}/BCP/Cu	1.08	22.0	77.2	16.45 ± 0.40	2019	136
	ITO/PTAA/$MAPbI_3$-DAP/C_{60}/BCP/Cu	1.18	22.5	81.7	20.53 ± 0.38	2019	136
	ITO/PTAA/$Cs_{0.2}FA_{0.8}Pb(I_{0.6}Br_{0.4})_3$/$C_{60}$/BCP/Cu	1.18	15.1	73.3	11.78 ± 0.57	2019	136
	ITO/PTAA/$Cs_{0.2}FA_{0.8}Pb(I_{0.6}Br_{0.4})_3$-DAP/$C_{60}$/BCP/Cu	1.26	15.6	77.5	13.87 ± 0.49	2019	136
	ITO/SnO_2/$FA_{0.98}Cs_{0.02}PEAPbI_3$/spiro-OMeTAD/Au	1.126	24.44	76.5	21.06	2018	71
	FTO/TiO_2/IDTBR–$(FAPbI_3)_{60}(BA_2PbBr_4)$/spiro-OMeTAD/Au	1.10	24.40	76.9	20.62	2018	137
	FTO/TiO_2/$Cs_{0.05}FA_{0.80}MA_{0.15}Pb(I_{0.85}Br_{0.15})_3$/s piro-OMeTAD/Au (0% EA)	21.92 ± 0.35	21.05 ± 0.31	71 ± 2	16.95 ± 0.42	2019	138
	FTO/TiO_2/$Cs_{0.05}FA_{0.80}MA_{0.15}Pb(I_{0.85}Br_{0.15})_3$/s piro-OMeTAD/Au (1% EA)	21.92 ± 0.35	21.05 ± 0.31	71 ± 1	18.02 ± 0.66	2019	138
	FTO/TiO_2/$Cs_{0.05}FA_{0.80}MA_{0.15}Pb(I_{0.85}Br_{0.15})_3$/s piro-OMeTAD/Au (2% EA)	1.15 ± 0.01	21.99 ± 0.29	72 ± 1	18.19 ± 0.53	2019	138
	FTO/TiO_2/$Cs_{0.05}FA_{0.80}MA_{0.15}Pb(I_{0.85}Br_{0.15})_3$/s piro-OMeTAD/Au (3% EA)	1.14 ± 0.01	21.92 ± 0.35	73 ± 2	18.38 ± 0.69	2019	138
	FTO/TiO_2/$Cs_{0.05}FA_{0.80}MA_{0.15}Pb(I_{0.85}Br_{0.15})_3$/s piro-OMeTAD/Au (4% EA)	1.10 ± 0.01	21.92 ± 0.35	72 ± 2	17.39 ± 0.48	2019	138
	FTO/TiO_2/$Cs_{0.05}FA_{0.80}MA_{0.15}Pb(I_{0.85}Br_{0.15})_3$/s piro-OMeTAD/Au (1% PA)	1.14 ± 0.01	21.80 ± 0.21	66 ± 2	16.37 ± 0.44	2019	138
	FTO/TiO_2/$Cs_{0.05}FA_{0.80}MA_{0.15}Pb(I_{0.85}Br_{0.15})_3$/s piro-OMeTAD/Au (2% PA)	1.14 ± 0.01	21.80 ± 0.21	66 ± 2	17.46 ± 0.68	2019	138
	FTO/TiO_2/$Cs_{0.05}FA_{0.80}MA_{0.15}Pb(I_{0.85}Br_{0.15})_3$/s piro-OMeTAD/Au (3% PA)	1.14 ± 0.01	22.12 ± 0.31	73 ± 1	17.46 ± 0.68	2019	138
	FTO/TiO_2/$Cs_{0.05}FA_{0.80}MA_{0.15}Pb(I_{0.85}Br_{0.15})_3$/s piro-OMeTAD/Au (4% PA)	1.14 ± 0.02	22.01 ± 0.25	70 ± 2	17.46 ± 0.68	2019	138
	FTO/TiO_2/$Cs_{0.05}FA_{0.80}MA_{0.15}Pb(I_{0.85}Br_{0.15})_3$/s piro-OMeTAD/Au (2% BA)	1.14 ± 0.01	22.02 ± 0.34	72 ± 1	18.00 ± 0.55	2019	138
	FTO/TiO_2/$Cs_{0.05}FA_{0.80}MA_{0.15}Pb(I_{0.85}Br_{0.15})_3$/s piro-OMeTAD/Au (3% BA)	1.14 ± 0.02	21.59 ± 0.19	70 ± 2	17.32 ± 0.46	2019	138
	FTO/TiO_2/$(CEA_2PbX_4)_x[(Cs_{0.1}FA_{0.9})Pb(I_{0.9}Br_{0.1})_3]_{1-x}$/s piro-OMeTAD/Au (FA)	1.06 ± 0.02	22.05 ± 0.88	76.03 ± 1.04	17.75 ± 1.22	2019	139
	FTO/TiO_2/$(CEA_2PbX_4)_x[(Cs_{0.1}FA_{0.9})Pb(I_{0.9}Br_{0.1})_3]_{1-x}$/s piro-OMeTAD/Au (3% CEA)	1.07 ± 0.02	22.29 ± 0.62	78.93 ± 0.71	18.78 ± 1.03	2019	139
	FTO/TiO_2/$(CEA_2PbX_4)_x[(Cs_{0.1}FA_{0.9})Pb(I_{0.9}Br_{0.1})_3]_{1-x}$/s piro-OMeTAD/Au (5% CEA)	1.09 ± 0.01	18.78 ± 1.03	79.04 ± 0.95	19.15 ± 0.93	2019	139
	FTO/TiO_2/$(CEA_2PbX_4)_x[(Cs_{0.1}FA_{0.9})Pb(I_{0.9}Br_{0.1})_3]_{1-x}$/s piro-OMeTAD/Au (9% CEA)	1.08 ± 0.04	20.87 ± 1.08	75.98 ± 1.71	17.58 ± 1.34	2019	139

Table 1 (*Contd.*)

PSCs	Structure	V_{OC} (mV)	J_{SC} (mA cm^{-2})	FF (%)	η (%)	Year	Ref
	FTO/TiO_2/$(CEA_2PbX_4)_x[(Cs_{0.1}FA_{0.9})Pb(I_{0.9}Br_{0.1})_3]_{1-x}$/s piro-OMeTAD/Au (15% CEA)	1.10 ± 0.02	19.81 ± 1.31	67.16 ± 2.81	14.49 ± 2.07	2019	139
	FTO/PEDOT:PSS/$GAMA_3Pb_3I_{10}$/PCBM/Al	0.974	9.36	79.7	7.26	2017	116
	ITO/PEDOT:PSS/$(GA)(MA)_3Pb_3I_{10}$/PCBM/Li–F/Al	1.08	20.75	74.52	16.65	2019	117
	FTO/c-TiO_2/$(GA)(MA)_3Pb_3I_{10}$/PCBM/Ag	1.15	18.8	67.8	14.7	2019	118
	FTO/c-TiO_2/$(GA)(MA)_3Pb_3I_{10}$/spiro-OMeTAD/Au	1.14	22.26	72.67	18.48	2019	119
	FTO/c-TiO_2/$(GA)(MA)_3Pb_3I_{10}$/spiro-OMeTAD/Au	1.08	22.68	78.01	19.18	2021	120
	FTO/PEDOT:PSS/$CsSnBrI_2$-PS/PCBM/BCP/Ag	0.43	17.2	68.7	5.01	2021	121
	ITO/PEDOT:PSS/$FASnI_3$/ICBA/BCP/Al	0.84	24.91	70.76	14.81	2021	122
	ITO/PEDOT:PSS/$FASnI_3$/C60/BCP/Ag	0.656	22.19	73.11	10.61	2022	123
	ITO/PEDOT:PSS/$PEA_{0.15}FA_{0.75}MA_{0.1}SnI_2Br$/PCBM/BCP/Ag	0.67	16.89	70.36	7.96	2022	124
	FTO/c-TiO_2/$(PEA)_2(MA)_2Pb_3I_{10}$/spiro-OMeTAD/Au	1.18	6.72	60	4.73	2014	125
	FTO/mp-TiO_2/$(BA)_2(MA)_2Pb_3I_{10}$/spiro-OMeTAD/Au	0.93	9.42	46	4.02	2015	126
	FTO/mp-TiO_2/$(BA)_2(MA)_3Pb_4I_{13}$/spiro-OMeTAD/Au	0.87	9.09	30	2.39	2015	126
	FTO/mp-TiO_2/$(IC_2H_4NH_3)_2(MA)_{n-1}Pb_nI_{3n+1}$/spiro-OMeTAD/Au	0.893	14.33	63	9.03	2016	127
	FTO/mp-TiO_2/mp-ZrO_2/$(AVA)_x(MA)_{1-x}PbI_3$/carbon	0.85	21.78	64	11.86	2017	128
	FTO/mp-TiO_2/$(PEA)_2(MA)_{49}Pb_{50}Br_{151}$/spiro-OMeTAD/Au	1.46	9.0	65	8.5	2017	129
	FTO/mp-TiO_2/$(PPA)_2(MA)_{49}Pb_{50}Br_{151}$/spiro-OMeTAD/Au	1.24	9.5	60	7.1	2017	130
	FTO/mp-TiO_2/$(BZA)_2(MA)_{49}Pb_{50}Br_{151}$/spiro-OMeTAD/Au	1.35	11.5	63	9.5	2017	130
	FTO/mp-TiO_2/$(EDA)(MA)_2[Pb_3I_{10}]$/spiro-OMeTAD/Au	1.24	16.57	56	11.58	2016	131
	ITO/PEDOT:PSS/$(PEI)_2(MA)_6Pb_7I_{22}$/PCBM/LiF/Ag	1.1	13.12	65	9.39	2016	132
	FTO/PEDOT:PSS/$(BA)_2(MA)_3Pb_4I_{13}$ (HC)/PCBM/Al	1.01	16.76	74	12.51	2016	133
	ITO/C_{60}/$(iso\text{-}BA)_2(MA)_3Pb_4I_{13}$ (HC)/spiro-OMeTAD/Au	1.20	16.54	53	10.63	2017	134
	FTO/m-TiO_2/$(BA)_2(MA)_3Sn_4I_{13}$/PTAA:TPFB/Au	0.23	24.1	46	2.53	2017	92
	ITO/NiO_x/$PEA_2FA_8Sn_9I_{28}$/PCBM/Al	0.59	14.44	69	5.94	2017	88
	ITO/PEDOT:PSS/$(PEA)_2(FA)_{n-1}Sn_nI_{3n+1}$/$C_{60}$/BCP/Al	0.458	22.5	58	9.0	2018	135
	ITO/PTAA/ $Cs_{0.05}FA_{0.70}MA_{0.25}PbI_3$/$C_{60}$/BCP/Cu	1.06	23.4	68.4	15.02 ± 0.78	2019	136
	ITO/PTAA/ $Cs_{0.05}FA_{0.70}MA_{0.25}PbI_3$-DAP/$C_{60}$/BCP/Cu	1.16	23.4	79.4	20.36 ± 0.46	2019	136
	ITO/PTAA/$MAPbI_3$/C_{60}/BCP/Cu	1.08	22.0	77.2	16.45 ± 0.40	2019	136
	ITO/PTAA/$MAPbI_3$-DAP/C_{60}/BCP/Cu	1.18	22.5	81.7	20.53 ± 0.38	2019	136
	ITO/PTAA/$Cs_{0.2}FA_{0.8}Pb(I_{0.6}Br_{0.4})_3$/$C_{60}$/BCP/Cu	1.18	15.1	73.3	11.78 ± 0.57	2019	136
	ITO/PTAA/$Cs_{0.2}FA_{0.8}Pb(I_{0.6}Br_{0.4})_3$-DAP/$C_{60}$/BCP/Cu	1.26	15.6	77.5	13.87 ± 0.49	2019	136
	ITO/SnO_2/$FA_{0.98}Cs_{0.02}PEAPbI_3$/spiro-OMeTAD/Au	1.126	24.44	76.5	21.06	2018	71
	FTO/TiO_2/IDTBR –$(FAPbI_3)_{60}(BA_2PbBr_4)$/spiro-OMeTAD/Au	1.10	24.40	76.9	20.62	2018	137
	FTO/TiO_2/$Cs_{0.05}FA_{0.80}MA_{0.15}Pb(I_{0.85}Br_{0.15})_3$/s piro-OMeTAD/Au (0% EA)	21.92 ± 0.35	21.05 ± 0.31	71 ± 2	16.95 ± 0.42	2019	138
	FTO/TiO_2/$Cs_{0.05}FA_{0.80}MA_{0.15}Pb(I_{0.85}Br_{0.15})_3$/s piro-OMeTAD/Au (1% EA)	21.92 ± 0.35	21.05 ± 0.31	71 ± 1	18.02 ± 0.66	2019	138
	FTO/TiO_2/$Cs_{0.05}FA_{0.80}MA_{0.15}Pb(I_{0.85}Br_{0.15})_3$/s piro-OMeTAD/Au (2% EA)	1.15 ± 0.01	21.99 ± 0.29	72 ± 1	18.19 ± 0.53	2019	138
	FTO/TiO_2/$Cs_{0.05}FA_{0.80}MA_{0.15}Pb(I_{0.85}Br_{0.15})_3$/s piro-OMeTAD/Au (3% EA)	1.14 ± 0.01	21.92 ± 0.35	73 ± 2	18.38 ± 0.69	2019	138
	FTO/TiO_2/$Cs_{0.05}FA_{0.80}MA_{0.15}Pb(I_{0.85}Br_{0.15})_3$/s piro-OMeTAD/Au (4% EA)	1.10 ± 0.01	21.92 ± 0.35	72 ± 2	17.39 ± 0.48	2019	138
	FTO/TiO_2/$Cs_{0.05}FA_{0.80}MA_{0.15}Pb(I_{0.85}Br_{0.15})_3$/s piro-OMeTAD/Au (1% PA)	1.14 ± 0.01	21.80 ± 0.21	66 ± 2	16.37 ± 0.44	2019	138
	FTO/TiO_2/$Cs_{0.05}FA_{0.80}MA_{0.15}Pb(I_{0.85}Br_{0.15})_3$/s piro-OMeTAD/Au (2% PA)	1.14 ± 0.01	21.80 ± 0.21	66 ± 2	17.46 ± 0.68	2019	138
	FTO/TiO_2/$Cs_{0.05}FA_{0.80}MA_{0.15}Pb(I_{0.85}Br_{0.15})_3$/s piro-OMeTAD/Au (3% PA)	1.14 ± 0.01	22.12 ± 0.31	73 ± 1	17.46 ± 0.68	2019	138
	FTO/TiO_2/$Cs_{0.05}FA_{0.80}MA_{0.15}Pb(I_{0.85}Br_{0.15})_3$/s piro-OMeTAD/Au (4% PA)	1.14 ± 0.02	22.01 ± 0.25	70 ± 2	17.46 ± 0.68	2019	138
	FTO/TiO_2/$Cs_{0.05}FA_{0.80}MA_{0.15}Pb(I_{0.85}Br_{0.15})_3$/s piro-OMeTAD/Au (2% BA)	1.14 ± 0.01	22.02 ± 0.34	72 ± 1	18.00 ± 0.55	2019	138
	FTO/TiO_2/$Cs_{0.05}FA_{0.80}MA_{0.15}Pb(I_{0.85}Br_{0.15})_3$/s piro-OMeTAD/Au (3% BA)	1.14 ± 0.02	21.59 ± 0.19	70 ± 2	17.32 ± 0.46	2019	138
	FTO/TiO_2/$(CEA_2PbX_4)_x[(Cs_{0.1}FA_{0.9})Pb(I_{0.9}Br_{0.1})_3]_{1-x}$/s piro-OMeTAD/Au (FA)	1.06 ± 0.02	22.05 ± 0.88	76.03 ± 1.04	17.75 ± 1.22	2019	139
	FTO/TiO_2/$(CEA_2PbX_4)_x[(Cs_{0.1}FA_{0.9})Pb(I_{0.9}Br_{0.1})_3]_{1-x}$/s piro-OMeTAD/Au (3% CEA)	1.07 ± 0.02	22.29 ± 0.62	78.93 ± 0.71	18.78 ± 1.03	2019	139
	FTO/TiO_2/$(CEA_2PbX_4)_x[(Cs_{0.1}FA_{0.9})Pb(I_{0.9}Br_{0.1})_3]_{1-x}$/s piro-OMeTAD/Au (5% CEA)	1.09 ± 0.01	18.78 ± 1.03	79.04 ± 0.95	19.15 ± 0.93	2019	139

Table 1 (*Contd.*)

PSCs	Structure	V_{OC} (mV)	J_{SC} (mA cm^{-2})	FF (%)	η (%)	Year	Ref
	FTO/TiO_2/$(CEA_2PbX_4)_x[(Cs_{0.1}FA_{0.9})Pb(I_{0.9}Br_{0.1})_3]_{1-x}$/s piro-OMeTAD/Au (9% CEA)	1.08 ± 0.04	20.87 ± 1.08	75.98 ± 1.71	17.58 ± 1.34	2019	139
	FTO/TiO_2/$(CEA_2PbX_4)_x[(Cs_{0.1}FA_{0.9})Pb(I_{0.9}Br_{0.1})_3]_{1-x}$/s piro-OMeTAD/Au (15% CEA)	1.10 ± 0.02	19.81 ± 1.31	67.16 ± 2.81	14.49 ± 2.07	2019	139
	FTO/TiO_2/$(CEA_2PbX_4)_x[(Cs_{0.1}FA_{0.9})Pb(I_{0.9}Br_{0.1})_3]_{1-x}$/s piro-OMeTAD/Au (3% BEA)	1.08 ± 0.01	22.16 ± 0.74	77.87 ± 0.68	18.66 ± 0.86	2019	139
	FTO/TiO_2/$(CEA_2PbX_4)_x[(Cs_{0.1}FA_{0.9})Pb(I_{0.9}Br_{0.1})_3]_{1-x}$/ Spiro-OMeTAD/Au (5% BEA)	1.10 ± 0.01	21.97 ± 0.64	78.58 ± 0.99	18.89 ± 1.06	2019	139
	FTO/TiO_2/$(CEA_2PbX_4)_x[(Cs_{0.1}FA_{0.9})Pb(I_{0.9}Br_{0.1})_3]_{1-x}$/s piro-OMeTAD/Au (9% BEA)	1.10 ± 0.02	20.34 ± 1.18	75.83 ± 1.58	16.99 ± 1.61	2019	139
	FTO/TiO_2/$(CEA_2PbX_4)_x[(Cs_{0.1}FA_{0.9})Pb(I_{0.9}Br_{0.1})_3]_{1-x}$/s piro-OMeTAD/Au (15% BEA)	1.11 ± 0.03	19.02 ± 1.65	69.68 ± 1.89	14.52 ± 2.16	2019	139
	FTO/TiO_2/FAMACsTBABPbI_XBr_{3-X}/spiro-OMeTAD/Au (TBAB 0 mM)	1.097	21.49	74.47	17.56	2020	140
	FTO/TiO_2/FAMACsTBABPbI_XBr_{3-X}/spiro-OMeTAD/Au (TBAB 5 mM)	1.114	22.45	72.89	18.24	2020	140
	FTO/TiO_2/FAMACsTBABPbI_XBr_{3-X}/spiro-OMeTAD/Au (TBAB 7.5 mM)	1.119	23.41	76.97	20.16	2020	140
	FTO/TiO_2/FAMACsTBABPbI_XBr_{3-X}/spiro-OMeTAD/Au (TBAB 10 mM)	1.116	21.93	76.49	18.72	2020	140
	FTO/TiO_2/FAMACsTBABPbI_XBr_{3-X}/spiro-OMeTAD/Au (TBAB 15 mM)	1.096	21.63	64.98	15.42	2020	140
	ITO/PTAA/PFN/NMA-$MAPbI_3$/PCBM/BCP/Cu (NMA vol. 0%)	1.07 (±0.01)	21.2 (±0.4)	80 (±01)	18.1 (±0.6)	2020	141
	ITO/PTAA/PFN/NMA-$MAPbI_3$/PCBM/BCP/Cu (NMA vol. 0.05%)	1.10 (±0.01)	21.2 (±0.4)	79 (±1)	18.7 (±0.5)	2020	141
	ITO/PTAA/PFN/NMA-$MAPbI_3$/PCBM/BCP/Cu (NMA vol. 0.10%)	1.13 (±0.01)	21.4 (±0.5)	80 (±1)	18.7 (±0.5)	2020	141
	ITO/PTAA/PFN/NMA-$MAPbI_3$/PCBM/BCP/Cu (NMA vol. 0.25%)	1.15 (±0.01)	21.4 (±0.5)	80 (±2)	19.3 (±0.7)	2020	141
	ITO/PTAA/PFN/NMA-$MAPbI_3$/PCBM/BCP/Cu (NMA vol. 0.50%)	1.14 (±0.01)	17.7 (±0.6)	78 (±2)	15.7 (±0.6)	2020	141
	ITO/PTAA/PFN/NMA-$MAPbI_3$/PCBM/BCP/Cu (NMA vol. 1.00%)	1.14 (±0.01)	14.4 (±1.1)	69 (±1)	15.7 (±0.6)	2020	141

promising PV materials. The development of mixed-dimensional PSCs offers the solar energy sector great promise. Compared to conventional 3D PSCs, these PSCs, especially 1D/3D configurations, have shown remarkable improvements in both efficiency and stability. This development points to a promising future for solar energy production, with the potential to increase conversion efficiencies and extend operational lifespans. Future work must focus on scaling up production, carrying out demanding long-term stability tests, investigating novel materials, integrating these solar cells into current technologies, and establishing regulatory standards to realize this potential fully. Mixed-dimensional PSCs can potentially become a transformative force in the renewable energy sector if these challenges can be overcome. If this goal is achieved, they could provide clean and efficient power solutions for various applications.

The dimensions of PSCs present a range of opportunities and challenges. Although they are flexible and inexpensive to fabricate, thin-film PSCs have problems with stability and scalability. On the other hand, thick-film cells struggle with uniform deposition and charge transport, but they also offer higher absorption and improved stability. PSCs with nanostructures, like those with nanowires, improve stability and charge collection but call for exact manufacturing and scalability issues to be resolved. Combining materials in tandem perovskite cells has the potential to increase efficiency, but there are cost and integration challenges. To fully utilize PSCs in sustainable energy applications, it is imperative to tackle stability concerns, enhance fabrication processes, and guarantee scalability.

Conflicts of interest

There are no conflicts to declare.

Acknowledgements

This work was supported by the National Research Foundation of Korea (NRF) grant funded by the Korean government (MSIT) (No. RS-2022-00165798). No. 2308085MF211, Anhui Natural Science Foundation. The authors acknowledge support and funding of King Khalid University through the Research Center for Advanced Materials Science (RCAMS) under grant no: RCAMS/KKU/001-23.

References

1 Y. Ye, Y. Yin, Y. Chen, S. Li, L. Li and Y. Yamauchi, *Small*, 2023, 2208119.
2 G.-Y. Kim, K. Kim, H. J. Kim, H. S. Jung, I. Jeon and J.-W. Lee, *EcoMat*, 2023, **5**, e12319.
3 J. Zhao, Z. Zhang, G. Li, M. H. Aldamasy, M. Li and A. Abate, *Adv. Energy Mater.*, 2023, **13**, 2204233.
4 T. Xue, Z. Huang, P. Zhang, M. Su, X. Hu, T. Wu, B. Fan, G. Chen, G. Yu, W. Liu, X. Liu, Y. Zhang and Y. Song, *InfoMat*, 2022, **4**, e12358.
5 S. Aftab, M. Z. Iqbal, S. Hussain, F. Kabir, A. A. Al-Kahtani and H. H. Hegazy, *Adv. Funct. Mater.*, 2023, 2303449.
6 S. Aftab, A. Abbas, M. Z. Iqbal, S. Hussain, F. Kabir, H. H. Hegazy, F. Xu, J. H. Kim and B. S. Goud, *Mater. Today Energy*, 2023, 101366.

7 S. Aftab, M. Z. Iqbal, S. Hussain, H. H. Hegazy and M. A. Saeed, *Nano energy*, 2023, **108**, 108249.
8 S. Aftab, M. Z. Iqbal, F. Kabir and S. Azam, *Nanoscale*, 2023, **15**, 3610–3629.
9 S. Lan, B. Pan, Y. Liu, Z. Zhang, L. Zhang, B. Yu, Y. Fang and P. Wang, *Carbon Energy*, 2023, e318.
10 C. Liang, H. Gu, J. Xia, T. Liu, S. Mei, N. Zhang, Y. Chen and G. Xing, *Carbon Energy*, 2023, **5**, e251.
11 X. Yao, J. Duan, Y. Zhao, J. Zhang, Q. Guo, Q. Zhang, X. Yang, Y. Duan, P. Yang and Q. Tang, *Carbon Energy*, 2023, e387.
12 S. Aftab, M. Saeed, S. Hussain, F. Kabir, M. Aslam, A. H. Rajpar and A. G. Al-Sehemi, *Solar RRL*, 2023, 2300803.
13 X. Li, S. Aftab, A. Abbas, S. Hussain, M. Aslam, F. Kabir, H. S. Abd-Rabboh, H. Hegazy, F. Xu and M. Z. Ansari, *Nano Energy*, 2023, 108979.
14 S. Aftab, S. Hussain, F. Kabir, M. Aslam, A. H. Rajpar and A. G. Al-Sehemi, *Nano Energy*, 2023, 109112.
15 X. Zhang, Y. Tang, F. Zhang and C. S. Lee, *Adv. Energy Mater.*, 2016, **6**, 1502588.
16 M. Wang, C. Jiang, S. Zhang, X. Song, Y. Tang and H.-M. Cheng, *Nat. Chem.*, 2018, **10**, 667–672.
17 S. Aftab, X. Li, S. Hussain, M. Aslam, A. H. Rajpar and A. G. Al-Sehemi, *Chem. Eng. J.*, 2023, 148143.
18 S. Liu, V. P. Biju, Y. Qi, W. Chen and Z. Liu, *NPG Asia Mater.*, 2023, **15**, 27.
19 H. A. Dewi, H. Wang, J. Li, M. Thway, R. Sridharan, R. Stangl, F. Lin, A. G. Aberle, N. Mathews, A. Bruno and S. Mhaisalkar, *ACS Appl. Mater. Interfaces*, 2019, **11**, 34178–34187.
20 R. Vidal, J.-A. Alberola-Borràs, N. Sánchez-Pantoja and I. Mora-Seró, *Adv. Energy Sustainability Res.*, 2021, **2**, 2000088.
21 T. Okoroafor, A. Maalouf, S. Oez, V. Babu, B. Wilk and S. Resalati, *J. Cleaner Prod.*, 2022, **373**, 133665.
22 B. Parida, A. Singh, A. K. Kalathil Soopy, S. Sangaraju, M. Sundaray, S. Mishra, S. Liu and A. Najar, *Advanced Science*, 2022, **9**, 2200308.
23 E. Berger, M. Bagheri, S. Asgari, J. Zhou, M. Kokkonen, P. Talebi, J. Luo, A. F. Nogueira, T. Watson and S. G. Hashmi, *Sustainable Energy Fuels*, 2022, **6**, 2879–2900.
24 E. Rezaee, D. Kutsarov, B. Li, J. Bi and S. R. P. Silva, *Sci. Rep.*, 2022, **12**, 7411.
25 P. Roy, A. Ghosh, F. Barclay, A. Khare and E. Cuce, *Coatings*, 2022, **12**, 1089.
26 P. Čulík, K. Brooks, C. Momblona, M. Adams, S. Kinge, F. Maréchal, P. J. Dyson and M. K. Nazeeruddin, *ACS Energy Lett.*, 2022, **7**, 3039–3044.
27 B. Roose, E. M. Tennyson, G. Meheretu, A. Kassaw, S. A. Tilahun, L. Allen and S. D. Stranks, *Energy Environ. Sci.*, 2022, **15**, 3571–3582.
28 M. Cai, Y. Wu, H. Chen, X. Yang, Y. Qiang and L. Han, *Adv. Sci.*, 2017, **4**, 1600269.
29 D. Zhou, T. Zhou, Y. Tian, X. Zhu and Y. Tu, *J. Nanomater.*, 2018, **2018**, 8148072.
30 Y.-T. Huang, S. R. Kavanagh, D. O. Scanlon, A. Walsh and R. L. Z. Hoye, *Nanotechnology*, 2021, **32**, 132004.
31 Y. Tu, J. Wu, G. Xu, X. Yang, R. Cai, Q. Gong, R. Zhu and W. Huang, *Adv. Mater.*, 2021, **33**, 2006545.
32 L. K. Ono, E. J. Juarez-Perez and Y. Qi, *ACS Appl. Mater. Interfaces*, 2017, **9**, 30197–30246.
33 S. Mu, Q. Liu, P. Kidkhunthod, X. Zhou, W. Wang and Y. Tang, *Natl. Sci. Rev.*, 2021, **8**, nwaa178.
34 Z. Huang, P. Luo, S. Jia, H. Zheng and Z. Lyu, *J. Phys. Chem. Solids*, 2022, **167**, 110746.
35 Y. Liu, X. Liu, X. Li, H. Yuan and Y. Xue, *IRE Trans. Ind. Electron.*, 2022, **70**, 9169–9180.
36 S. Ye, J. Zhu, S. Zhu, Y. Zhao, M. Li, Z. Huang, H. Wang and J. He, *ACS Appl. Mater. Interfaces*, 2023, **15**, 47475–47486.
37 L. Meng, J. You and Y. Yang, *Nat. Commun.*, 2018, **9**, 5265.
38 M. Khalid and T. K. Mallick, *Energies*, 2023, **16**, 4031.
39 T. A. Chowdhury, M. A. Bin Zafar, M. Sajjad-Ul Islam, M. Shahinuzzaman, M. A. Islam and M. U. Khandaker, *RSC Adv.*, 2023, **13**, 1787–1810.
40 D. Zhang, D. Li, Y. Hu, A. Mei and H. Han, *Commun. Mater.*, 2022, **3**, 58.
41 A. S. R. Bati, Y. L. Zhong, P. L. Burn, M. K. Nazeeruddin, P. E. Shaw and M. Batmunkh, *Commun. Mater.*, 2023, **4**, 2.
42 M. I. H. Ansari, A. Qurashi and M. K. Nazeeruddin, *J. Photochem. Photobiol., C*, 2018, **35**, 1–24.
43 Q. Chen, N. De Marco, Y. Yang, T.-B. Song, C.-C. Chen, H. Zhao, Z. Hong, H. Zhou and Y. Yang, *Nano Today*, 2015, **10**, 355–396.
44 H. S. Jung, G. S. Han, N.-G. Park and M. J. Ko, *Joule*, 2019, **3**, 1850–1880.
45 S. A. Olaleru, J. K. Kirui, D. Wamwangi, K. T. Roro and B. Mwakikunga, *Sol. Energy*, 2020, **196**, 295–309.
46 J. Prakash, A. Singh, G. Sathiyan, R. Ranjan, A. Singh, A. Garg and R. K. Gupta, *Mater. Today Energy*, 2018, **9**, 440–486.
47 J. R. Harwell, T. K. Baikie, I. D. Baikie, J. L. Payne, C. Ni, J. T. S. Irvine, G. A. Turnbull and I. D. W. Samuel, *Phys. Chem. Chem. Phys.*, 2016, **18**, 19738–19745.
48 X. Zhu, Q. Xu, H. Li, M. Liu, Z. Li, K. Yang, J. Zhao, L. Qian, Z. Peng and G. Zhang, *Adv. Mater.*, 2019, **31**, 1902479.
49 H. Li, Z. Li, N. Li, X. Zhu, Y. F. Zhang, L. Sun, R. Wang, J. Zhang, Z. Yang and H. Yi, *Small*, 2022, **18**, 2107811.
50 H. Zhang, X. Zhu, Y. Tai, J. Zhou, H. Li, Z. Li, R. Wang, J. Zhang, Y. Zhang and W. Ge, *Int. J. Extreme Manuf.*, 2023, **5**, 032005.
51 C. Lu, R. Ren, Z. Zhu, G. Pan, G. Wang, C. Xu, J. Qiao, W. Sun, Q. Huang and H. Liang, *Chem. Eng. J.*, 2023, **472**, 144878.
52 T. Ibn-Mohammed, S. C. L. Koh, I. M. Reaney, A. Acquaye, G. Schileo, K. B. Mustapha and R. Greenough, *Renewable Sustainable Energy Rev.*, 2017, **80**, 1321–1344.
53 N. B. Correa Guerrero, W. O. Herrera Martínez, B. Civit and M. D. Perez, *Sol. Energy*, 2021, **230**, 645–653.
54 T. Wei, Y. Zhou, C. Sun, X. Guo, S. Xu, D. Chen and Y. Tang, *Nano Res.*, 2023, 1–7.
55 P. Xu, D. Lan, F. Wang and I. Shin, *Electronics*, 2023, **12**, 3155.
56 L. Wang, Y. Jiang, S.-Y. Li, X.-H. Chen, F.-S. Xi, X.-H. Wan, W.-H. Ma and R. Deng, *Rare Met.*, 2023, 1–12.

57 Z. Wang, J. Li, C. Hu, X. Li and Y. Zhu, *J. Energy Storage*, 2024, **75**, 109432.
58 D. Chen, Y. Zhu, S. Han, L. Anatoly, M. Andrey and L. Lu, *J. Energy Storage*, 2023, **60**, 106587.
59 Y. Lu, M. Stegmaier, P. Nukala, M. A. Giambra, S. Ferrari, A. Busacca, W. H. Pernice and R. Agarwal, *Nano Lett.*, 2017, **17**, 150–155.
60 J. Zhu, B. He, X. Yao, H. Chen, Y. Duan, J. Duan and Q. Tang, *Small*, 2022, **18**, 2106323.
61 B. A. Huisman, F. Palazon and H. J. Bolink, *Inorg. Chem.*, 2021, **60**, 5212–5216.
62 C. McDonald, C. Ni, V. Švrček, M. Lozac'h, P. A. Connor, P. Maguire, J. T. S. Irvine and D. Mariotti, *Nanoscale*, 2017, **9**, 18759–18771.
63 S. Öz, J.-C. Hebig, E. Jung, T. Singh, A. Lepcha, S. Olthof, F. Jan, Y. Gao, R. German and P. H. van Loosdrecht, *Sol. Energy Mater. Sol. Cells*, 2016, **158**, 195–201.
64 H. Liu, H. Han, J. Xu, X. Pan, K. Zhao, S. Liu and J. Yao, *Adv. Mater.*, 2023, 2300302.
65 J. Wang, L. Liu, S. Chen, L. Qi, M. Zhao, C. Zhao, J. Tang, X. Cai, F. Lu and T. Jiu, *Small*, 2022, **18**, 2104100.
66 P. Zardari and A. Rostami, *Sol. Energy Mater. Sol. Cells*, 2021, **227**, 111119.
67 M. Salado, M. Oliva-Ramirez, S. Kazim, A. R. González-Elipe and S. Ahmad, *Nano Energy*, 2017, **35**, 215–222.
68 Y. Zhang and N.-G. Park, *ACS Energy Lett.*, 2022, **7**, 757–765.
69 X. Zhang, G. Wu, W. Fu, M. Qin, W. Yang, J. Yan, Z. Zhang, X. Lu and H. Chen, *Adv. Energy Mater.*, 2018, **8**, 1702498.
70 M. Shao, T. Bie, L. Yang, Y. Gao, X. Jin, F. He, N. Zheng, Y. Yu and X. Zhang, *Adv. Mater.*, 2022, **34**, 2107211.
71 J.-W. Lee, Z. Dai, T.-H. Han, C. Choi, S.-Y. Chang, S.-J. Lee, N. De Marco, H. Zhao, P. Sun and Y. Huang, *Nat. Commun.*, 2018, **9**, 3021.
72 K. Hong, Q. Van Le, S. Y. Kim and H. W. Jang, *J. Mater. Chem. C*, 2018, **6**, 2189–2209.
73 T. He, S. Li, Y. Jiang, C. Qin, M. Cui, L. Qiao, H. Xu, J. Yang, R. Long and H. Wang, *Nat. Commun.*, 2020, **11**, 1672.
74 C. Gai, J. Wang, Y. Wang and J. Li, *Energies*, 2019, **13**, 2.
75 Y. Chen, B. Liu, Q. Zhou, D. Ma, X. Han, D. He, S. Chen, Y. Li, S. Lu and Z.-X. Xu, *J. Mater. Chem. A*, 2023, **11**, 18592–18604.
76 L. Liu, A. Najar, K. Wang, M. Du and S. Liu, *Advanced Science*, 2022, **9**, 2104577.
77 Z. Ding, S. Li, Y. Jiang, D. Wang and M. Yuan, *Nanoscale*, 2023, **15**, 3713–3729.
78 Q. Zhao, S. Wang, Y.-H. Kim, S. Mondal, Q. Miao, S. Li, D. Liu, M. Wang, Y. Zhai and J. Gao, *Green Energy Environ.*, 2023.
79 W. Chi and S. K. Banerjee, *Chem. Eng. J.*, 2021, **426**, 131588.
80 N. Zhou, D. Wang, Y. Bao, R. Zhu, P. Yang and L. Song, *Adv. Opt. Mater.*, 2023, 2202681.
81 M. Wang, F. Cao and L. Li, *Small Struct.*, 2022, **3**, 2100165.
82 S. Choon, H. Lim, I. Ibrahim, Z. Zainal, K. Tan, C. Foo and C. Ng, *Renewable Sustainable Energy Rev.*, 2023, **171**, 113037.
83 C. McDonald, C. Ni, V. Švrček, M. Lozac'h, P. A. Connor, P. Maguire, J. T. Irvine and D. Mariotti, *Nanoscale*, 2017, **9**, 18759–18771.
84 J. Wu, Y. Li, Y. Zhang, Y. Li, Y. Huang, Z. Jiang, Q. Ai, Y. Liu, L. Zhang and Y. Peng, *Small*, 2022, **18**, 2200130.
85 H. Jiao, Z. Ni, Z. Shi, C. Fei, Y. Liu, X. Dai and J. Huang, *Sci. Adv.*, 2022, **8**, eabq4524.
86 N. Wei, Y. Chen, X. Wang, Y. Miao, Z. Qin, X. Liu, H. Wei and Y. Zhao, *Adv. Funct. Mater.*, 2022, **32**, 2108944.
87 J. Chen, Y. Yang, H. Dong, J. Li, X. Zhu, J. Xu, F. Pan, F. Yuan, J. Dai and B. Jiao, *Sci. Adv.*, 2022, **8**, eabk2722.
88 Y. Liao, H. Liu, W. Zhou, D. Yang, Y. Shang, Z. Shi, B. Li, X. Jiang, L. Zhang and L. N. Quan, *J. Am. Chem. Soc.*, 2017, **139**, 6693–6699.
89 J. Qiu, Y. Xia, Y. Chen and W. Huang, *Advanced Science*, 2019, **6**, 1800793.
90 K. Chen, P. Wu, W. Yang, R. Su, D. Luo, X. Yang, Y. Tu, R. Zhu and Q. Gong, *Nano Energy*, 2018, **49**, 411–418.
91 M. Liao, B. B. Yu, Z. Jin, W. Chen, Y. Zhu, X. Zhang, W. Yao, T. Duan, I. Djerdj and Z. He, *ChemSusChem*, 2019, **12**, 5007–5014.
92 D. H. Cao, C. C. Stoumpos, T. Yokoyama, J. L. Logsdon, T.-B. Song, O. K. Farha, M. R. Wasielewski, J. T. Hupp and M. G. Kanatzidis, *ACS Energy Lett.*, 2017, **2**, 982–990.
93 N. Sun, W. Gao, H. Dong, X. Liu, L. Chao, W. Hui, Y. Xia, C. Ran and Y. Chen, *ACS Appl. Energy Mater.*, 2022, **5**, 4008–4016.
94 H. Xu, Y. Jiang, T. He, S. Li, H. Wang, Y. Chen, M. Yuan and J. Chen, *Adv. Funct. Mater.*, 2019, **29**, 1807696.
95 J. Qiu, Y. Xia, Y. Zheng, W. Hui, H. Gu, W. Yuan, H. Yu, L. Chao, T. Niu and Y. Yang, *ACS Energy Lett.*, 2019, **4**(7), 1513–1520.
96 M. Li, W.-W. Zuo, Y.-G. Yang, M. Aldamasy, Q. Wang, S. H. T. Cruz, S.-L. Feng, M. Saliba, Z.-K. Wang and A. Abate, *ACS Energy Lett.*, 2020, **5**, 1923–1929.
97 X. Jiang, H. Li, Q. Zhou, Q. Wei, M. Wei, L. Jiang, Z. Wang, Z. Peng, F. Wang and Z. Zang, *J. Am. Chem. Soc.*, 2021, **143**, 10970–10976.
98 J. Qiu, Y. Lin, X. Ran, Q. Wei, X. Gao, Y. Xia, P. Müller-Buschbaum and Y. Chen, *Sci. China: Chem.*, 2021, **64**, 1577–1585.
99 Y. Xu, K.-J. Jiang, P. Wang, W.-M. Gu, G.-H. Yu, X. Zhou and Y. Song, *New J. Chem.*, 2022, **46**, 2259–2265.
100 G. Li, Z. Su, M. Li, F. Yang, M. H. Aldamasy, J. Pascual, F. Yang, H. Liu, W. Zuo and D. Di Girolamo, *Adv. Energy Mater.*, 2021, **11**, 2101539.
101 M. Chen, M.-G. Ju, M. Hu, Z. Dai, Y. Hu, Y. Rong, H. Han, X. C. Zeng, Y. Zhou and N. P. Padture, *ACS Energy Lett.*, 2018, **4**, 276–277.
102 M. Chen, Q. Dong, F. T. Eickemeyer, Y. Liu, Z. Dai, A. D. Carl, B. Bahrami, A. H. Chowdhury, R. L. Grimm and Y. Shi, *ACS Energy Lett.*, 2020, **5**, 2223–2230.
103 P. Li, X. Liu, Y. Zhang, C. Liang, G. Chen, F. Li, M. Su, G. Xing, X. Tao and Y. Song, *Angew. Chem., Int. Ed.*, 2020, **59**, 6909–6914.
104 B. Ma, J. Chen, M. Wang, X. Xu, J. Qian, Y. Lu, W. Zhang, P. Xia, M. Qin and W. Zhu, *J. Phys. Chem. C*, 2020, **124**, 16289–16299.

105 W. Ke, C. Chen, I. Spanopoulos, L. Mao, I. Hadar, X. Li, J. M. Hoffman, Z. Song, Y. Yan and M. G. Kanatzidis, *J. Am. Chem. Soc.*, 2020, **142**, 15049–15057.
106 T. Xue, Z. Huang, P. Zhang, M. Su, X. Hu, T. Wu, B. Fan, G. Chen, G. Yu and W. Liu, *InfoMat*, 2022, **4**, e12358.
107 Y. Zhan, F. Yang, W. Chen, H. Chen, Y. Shen, Y. Li and Y. Li, *Adv. Mater.*, 2021, **33**, 2105170.
108 B. Zhao, J. Guo, C. Zhao, X. Zhang, H. Huang, Z. Tang, L. A. Frolova, P. A. Troshin, W. Ma and J. Yuan, *Adv. Funct. Mater.*, 2023, **33**, 2304161.
109 M. A. Mahmud, T. Duong, Y. Yin, H. T. Pham, D. Walter, J. Peng, Y. Wu, L. Li, H. Shen and N. Wu, *Adv. Funct. Mater.*, 2020, **30**, 1907962.
110 C. Wu, Y. Liu, H. Liu, C. Duan, Q. Pan, J. Zhu, F. Hu, X. Ma, T. Jiu and Z. Li, *J. Am. Chem. Soc.*, 2018, **140**, 10016–10024.
111 F. Zhang, H. Lu, B. W. Larson, C. Xiao, S. P. Dunfield, O. G. Reid, X. Chen, M. Yang, J. J. Berry and M. C. Beard, *Chem*, 2021, **7**, 774–785.
112 Y. Zhu, L. Shu, S. Poddar, Q. Zhang, Z. Chen, Y. Ding, Z. Long, S. Ma, B. Ren and X. Qiu, *Nano Lett.*, 2022, **22**, 9586–9595.
113 Y. Yu, J. Li, D. Geng, J. Wang, L. Zhang, T. L. Andrew, M. S. Arnold and X. Wang, *Acs Nano*, 2015, **9**, 564–572.
114 H. Lu, K. Deng, N. Yan, Y. Ma, B. Gu, Y. Wang and L. Li, *Sci. Bull.*, 2016, **61**, 778–786.
115 W. Ke, C. C. Stoumpos, M. Zhu, L. Mao, I. Spanopoulos, J. Liu, O. Y. Kontsevoi, M. Chen, D. Sarma and Y. Zhang, *Adv. Sci.*, 2017, **3**, e1701293.
116 C. M. M. Soe, C. C. Stoumpos, M. Kepenekian, B. Traoré, H. Tsai, W. Nie, B. Wang, C. Katan, R. Seshadri and A. D. Mohite, *J. Am. Chem. Soc.*, 2017, **139**, 16297–16309.
117 H. Gu, C. Liang, Y. Xia, Q. Wei, T. Liu, Y. Yang, W. Hui, H. Chen, T. Niu and L. Chao, *Nano Energy*, 2019, **65**, 104050.
118 Y. Zhang, P. Wang, M.-C. Tang, D. Barrit, W. Ke, J. Liu, T. Luo, Y. Liu, T. Niu and D.-M. Smilgies, *J. Am. Chem. Soc.*, 2019, **141**, 2684–2694.
119 T. Luo, Y. Zhang, Z. Xu, T. Niu, J. Wen, J. Lu, S. Jin, S. Liu and K. Zhao, *Adv. Mater.*, 2019, **31**, 1903848.
120 J. Yang, T. Yang, D. Liu, Y. Zhang, T. Luo, J. Lu, J. Fang, J. Wen, Z. Deng and S. Liu, *Sol. RRL*, 2021, **5**, 2100286.
121 B. B. Yu, Z. Chen, Y. Zhu, Y. Wang, B. Han, G. Chen, X. Zhang, Z. Du and Z. He, *Adv. Mater.*, 2021, **33**, 2102055.
122 H. Li, X. Jiang, Q. Wei, Z. Zang, M. Ma, F. Wang, W. Zhou and Z. Ning, *Angew. Chem.*, 2021, **133**, 16466–16472.
123 J. Sanchez-Diaz, R. S. Sánchez, S. Masi, M. Krečmarová, A. O. Alvarez, E. M. Barea, J. Rodriguez-Romero, V. S. Chirvony, J. F. Sánchez-Royo and J. P. Martinez-Pastor, *Joule*, 2022, **6**, 861–883.
124 S. Cho, P. Pandey, J. Park, T.-W. Lee, H. Ahn, H. Choi and D.-W. Kang, *Chem. Eng. J.*, 2022, **446**, 137388.
125 I. C. Smith, E. T. Hoke, D. Solis-Ibarra, M. D. McGehee and H. I. Karunadasa, *Angew. Chem., Int. Ed.*, 2014, **53**, 11232–11235.
126 D. H. Cao, C. C. Stoumpos, O. K. Farha, J. T. Hupp and M. G. Kanatzidis, *J. Am. Chem. Soc.*, 2015, **137**, 7843–7850.
127 T. M. Koh, V. Shanmugam, J. Schlipf, L. Oesinghaus, P. Müller-Buschbaum, N. Ramakrishnan, V. Swamy, N. Mathews, P. P. Boix and S. G. Mhaisalkar, *Adv. Mater.*, 2016, **28**, 3653–3661.
128 G. Grancini, C. Roldán-Carmona, I. Zimmermann, E. Mosconi, X. Lee, D. Martineau, S. Narbey, F. Oswald, F. De Angelis and M. Graetzel, *Nat. Commun.*, 2017, **8**, 15684.
129 B. E. Cohen, M. Wierzbowska and L. Etgar, *Adv. Funct. Mater.*, 2017, **27**, 1604733.
130 B.-E. Cohen, M. Wierzbowska and L. Etgar, *Sustainable Energy Fuels*, 2017, **1**, 1935–1943.
131 W. Jiang, J. Ying, W. Zhou, K. Shen, X. Liu, X. Gao, F. Guo, Y. Gao and T. Yang, *Chem. Phys. Lett.*, 2016, **658**, 71–75.
132 K. Yao, X. Wang, Y.-x. Xu, F. Li and L. Zhou, *Chem. Mater.*, 2016, **28**, 3131–3138.
133 H. Tsai, W. Nie, J.-C. Blancon, C. C. Stoumpos, R. Asadpour, B. Harutyunyan, A. J. Neukirch, R. Verduzco, J. J. Crochet and S. Tretiak, *Nature*, 2016, **536**, 312–316.
134 Y. Chen, Y. Sun, J. Peng, W. Zhang, X. Su, K. Zheng, T. Pullerits and Z. Liang, *Adv. Energy Mater.*, 2017, **7**, 1700162.
135 S. Shao, J. Liu, G. Portale, H. H. Fang, G. R. Blake, G. H. ten Brink, L. J. A. Koster and M. A. Loi, *Adv. Energy Mater.*, 2018, **8**, 1702019.
136 W.-Q. Wu, Z. Yang, P. N. Rudd, Y. Shao, X. Dai, H. Wei, J. Zhao, Y. Fang, Q. Wang and Y. Liu, *Adv. Sci.*, 2019, **5**, eaav8925.
137 T. Niu, J. Lu, M.-C. Tang, D. Barrit, D.-M. Smilgies, Z. Yang, J. Li, Y. Fan, T. Luo and I. McCulloch, *Energy Environ. Sci.*, 2018, **11**, 3358–3366.
138 C. Fei, M. Zhou, J. Ogle, D.-M. Smilgies, L. Whittaker-Brooks and H. Wang, *J. Mater. Chem. A*, 2019, **7**, 23739–23746.
139 G. Liu, H. Zheng, X. Xu, S. Xu, X. Zhang, X. Pan and S. Dai, *Adv. Funct. Mater.*, 2019, **29**, 1807565.
140 S. Jin, Y. Wei, B. Rong, Y. Fang, Y. Zhao, Q. Guo, Y. Huang, L. Fan and J. Wu, *J. Power Sources*, 2020, **450**, 227623.
141 C. T. Lin, J. Lee, J. Kim, T. J. Macdonald, J. Ngiam, B. Xu, M. Daboczi, W. Xu, S. Pont and B. Park, *Adv. Funct. Mater.*, 2020, **30**, 1906763.
142 J. Duan, Y. Zhao, B. He and Q. Tang, *Angew. Chem., Int. Ed.*, 2018, **57**, 3787–3791.
143 K. Tvingstedt, O. Malinkiewicz, A. Baumann, C. Deibel, H. J. Snaith, V. Dyakonov and H. J. Bolink, *Sci. Rep.*, 2014, **4**, 6071.
144 J. Yao, T. Kirchartz, M. S. Vezie, M. A. Faist, W. Gong, Z. He, H. Wu, J. Troughton, T. Watson and D. Bryant, *Phys. Rev. Appl.*, 2015, **4**, 014020.
145 C. Ma, D. Shen, B. Huang, X. Li, W.-C. Chen, M.-F. Lo, P. Wang, M. H.-W. Lam, Y. Lu and B. Ma, *J. Mater. Chem. A*, 2019, **7**, 8811–8817.
146 C. Ma, D. Shen, B. Huang, X. Li, W.-C. Chen, M.-F. Lo, P. Wang, M. Hon-Wah Lam, Y. Lu, B. Ma and C.-S. Lee, *J. Mater. Chem. A*, 2019, **7**, 8811–8817.
147 D.-H. Kang and N.-G. Park, *Adv. Mater.*, 2019, **31**, 1805214.
148 J. Lee, Z. Dai, T. Han, C. Choi, S. Chang, S. Lee, N. De Marco, H. Zhao, P. Sun and Y. Huang, *Nat. Commun.*, 2018, **9**(1), 3021.

149 F. Zheng, C. Zuo, M. Niu, C. Zhou, S. J. Bradley, C. R. Hall, W. Xu, X. Wen, X. Hao and M. Gao, *ACS Appl. Mater. Interfaces*, 2020, **12**, 25980–25990.
150 H. Kim, M. Pei, Y. Lee, A. A. Sutanto, S. Paek, V. I. Queloz, A. J. Huckaba, K. T. Cho, H. J. Yun and H. Yang, *Adv. Funct. Mater.*, 2020, **30**, 1910620.
151 P. Li, Y. Zhang, C. Liang, G. Xing, X. Liu, F. Li, X. Liu, X. Hu, G. Shao and Y. Song, *Adv. Mater.*, 2018, **30**, 1805323.
152 S. Gharibzadeh, B. Abdollahi Nejand, M. Jakoby, T. Abzieher, D. Hauschild, S. Moghadamzadeh, J. A. Schwenzer, P. Brenner, R. Schmager and A. A. Haghighirad, *Adv. Energy Mater.*, 2019, **9**, 1803699.
153 M. Dehghanipour, A. Behjat and H. A. Bioki, *J. Mater. Chem. C*, 2021, **9**, 957–966.
154 T. Zhou, Z. Xu, R. Wang, X. Dong, Q. Fu and Y. Liu, *Adv. Mater.*, 2022, **34**, 2200705.
155 A. A. Sutanto, R. Szostak, N. Drigo, V. I. Queloz, P. Marchezi, J. Germino, H. C. Tolentino, M. K. Nazeeruddin, A. F. Nogueira and G. Grancini, *Nano Lett.*, 2020, **20**, 3992–3998.
156 M.-G. La-Placa, L. Gil-Escrig, D. Guo, F. Palazon, T. J. Savenije, M. Sessolo and H. J. Bolink, *ACS Energy Lett.*, 2019, **4**, 2893–2901.
157 X. Jiang, J. Zhang, S. Ahmad, D. Tu, X. Liu, G. Jia, X. Guo and C. Li, *Nano Energy*, 2020, **75**, 104892.